Rab10 regulates neuropeptide release by maintaining Ca^{2+} homeostasis and protein synthesis

Jian Dong[1], Miao Chen[2], Jan R. T. van Weering[3], Ka Wan Li[2], August B Smit[2], Ruud F. Toonen[1], Matthijs Verhage[1,3*]

[1] Department of Functional Genomics, Center for Neurogenomics and Cognitive Research (CNCR), Vrije Universiteit (VU) Amsterdam; Amsterdam 1081 HV, the Netherlands

[2] Department of Molecular and Cellular Neurobiology, Center for Neurogenomics and Cognitive Research (CNCR), Vrije Universiteit (VU) Amsterdam; Amsterdam 1081 HV, the Netherlands

[3] Department of Clinical Genetics, Center for Neurogenomics and Cognitive Research (CNCR), University Medical Center Amsterdam; Amsterdam 1081 HV, the Netherlands

*Corresponding author: matthijs@cncr.vu.nl

Keywords: Neuropeptide; exocytosis; Rab10; protein synthesis; ER, synaptic transmission

The authors declare no conflict of interest.

Abstract

Dense core vesicles (DCVs) transport and release various neuropeptides and neurotrophins that control diverse brain functions, but the DCV secretory pathway remains poorly understood. Here, we tested a prediction emerging from invertebrate studies about the crucial role of the intracellular trafficking GTPase Rab10, by assessing DCV exocytosis at single-cell resolution upon acute Rab10 depletion in mature mouse hippocampal neurons, to circumvent potential confounding effects of Rab10's established role in neurite outgrowth. We observed a significant inhibition of DCV exocytosis in Rab10-depleted neurons, whereas synaptic vesicle exocytosis was unaffected. However, rather than a direct involvement in DCV trafficking, this effect was attributed to two ER-dependent processes, ER-regulated intracellular Ca^{2+} dynamics and protein synthesis. Gene ontology analysis of differentially expressed proteins upon Rab10 depletion identified substantial alterations in synaptic and ER/ribosomal proteins, including the Ca^{2+}-pump SERCA2. In addition, ER morphology and dynamics were altered, ER Ca^{2+} levels were depleted and Ca^{2+} homeostasis was impaired in Rab10-depleted neurons. However, Ca^{2+} entry using a Ca^{2+} ionophore still triggered less DCV exocytosis. Instead, leucine supplementation, which enhances protein synthesis, largely rescued DCV exocytosis deficiency. We conclude that Rab10 is required for neuropeptide release by maintaining Ca^{2+} dynamics and regulating protein synthesis. Furthermore, DCV exocytosis appeared more dependent on (acute) protein synthesis than synaptic vesicle exocytosis.

Introduction

Dense core vesicles (DCVs) transport and release neuromodulators (neuropeptides, neurotrophic factors, and catecholamines) that play crucial roles in modulating diverse brain functions, including sleep, mood, memory, and learning (e.g., Cawley et al., 2016; Malva et al., 2012; Poo, 2001; Salio et al., 2006). Deficits in neuropeptide signaling pathways have been associated with several human disorders and diseases, including anxiety, depression, and obesity (Beck, 2000; Sah and Geracioti, 2013; Barde et al., 2022). Neuropeptides are synthesized in the endoplasmic reticulum (ER) and subsequently packaged into immature DCVs in the Golgi complex (Tooze et al., 2001). DCVs are transported along the neurites and undergo activity-dependent membrane fusion with the plasma membrane to release their content (Farina et al., 2015; Heidelberger et al., 1994; Nassal et al., 2022; Thomas et al., 1993; van de Bospoort et al., 2012). Despite the critical role of neuropeptides in brain functions, the regulatory mechanisms governing their secretion are not fully understood. We have shown previously that Rab3 is an essential regulator in the last steps of the DCV secretory pathway in mammalian neurons (Persoon et al., 2019). However, studies in invertebrates have also implicated other Rab proteins, including Rab2, Rab5, and Rab10, in the DCV secretory pathway: (Ailion et al., 2014; Azouz et al., 2014; Edwards et al., 2009; Hannemann et al., 2012; Lund et al., 2020; Sasidharan et al., 2012; Sumakovic et al., 2009).

Among these Rab proteins, Rab10 deficiency produces the strongest inhibition of neuropeptide release in *C. elegans* (Sasidharan et al., 2012). With its subcellular localization in many vesicular organelles, such as plasmalemmal precursor vesicles (PPVs), GLUT4 transport vesicles, and recycling endosomes, Rab10 regulates various aspects of intracellular membrane trafficking, including vesicle formation, transport, and fusion (Chen et al., 2006; Larance et al., 2005; Mîinea et al., 2005; Sano et al., 2007; Taylor et al., 2015). Rab10 deficiency leads to deficits in these pathways, resulting in impaired neuronal outgrowth and disrupted retrograde axonal transport of signaling factors (Lazo and Schiavo, 2023). How these deficits relate to the strong inhibition of DCV exocytosis remains unknown.

Deletion of Rab10 expression or inhibiting its functions by overexpression of an inactive mutant (Rab10T23N) leads to abnormal ER morphology (English and Voeltz, 2013; Lv et al., 2015; Shih and Hsueh, 2016). Since the ER is a crucial organelle involved in protein synthesis, Ca^{2+} buffering, and lipid metabolism, alterations in its structure and function can

73 directly or indirectly affect neuronal secretory pathways. Indeed, several studies have
74 suggested the roles of the ER in the DCV pathway, such as the involvement of ER stress and
75 lipid levels in DCV production in *C. elegans* (Laurent et al., 2018; Valadas et al., 2018), and
76 the roles of ER Ca^{2+} as an internal Ca^{2+} source regulating somatodendritic dopamine release
77 in mouse substantia nigra neurons (Patel et al., 2009). Additionally, Rab10 mutations, altered
78 expression levels, or phosphorylation states are firmly associated with CNS disorders (Agola
79 et al., 2011; Cheng et al., 2005; Ishida et al., 2016; Kiral et al., 2018). Hence, the strong
80 inhibition of neuropeptide accumulation in coelomocytes in nematode Rab10 mutants may be
81 a direct or indirect effect of Rab10 loss of function on DCV exocytosis and Rab10-dependent
82 disease processes may (in part) be explained by DCV exocytosis impairment.
83
84 In the present study, we investigated the involvement of Rab10 in regulated secretion of
85 neuropeptides in mammalian neurons. We directly assessed DCV exocytosis at single-cell
86 resolution in mouse hippocampal neurons and confirmed that Rab10 is a crucial regulator of
87 DCV exocytosis also in mammalian systems, while not affecting synaptic vesicle (SV)
88 exocytosis. However, instead of having a direct role in the DCV secretory pathway, we
89 observed that Rab10 is involved in DCV exocytosis through ER-dependent processes,
90 especially reduced ER Ca^{2+} homeostasis and impaired global protein synthesis.
91 Supplementation with leucine known to boost protein synthesis, rescued the defects in DCV
92 exocytosis. We therefore conclude that Rab10 plays a central role in regulating DCV
93 exocytosis by maintaining Ca^{2+} homeostasis and protein synthesis.

Results

Rab10 regulates neuronal outgrowth but is dispensable for synaptogenesis and SV exocytosis under intense stimulation

To study the role of Rab10 in regulated secretion, we utilized a knockdown strategy since complete knockout of Rab10 results in lethality at cell and organismal levels (Lv et al., 2015). We selected two specific shRNA sequences, shRNA#9, and shRNA#11, to deplete Rab10 expression, and a scrambled sequence as control. In mouse cortical neurons infected with either shRNA#9 or shRNA#11 at day in vitro 0 (DIV0), we observed a 75-95% decrease in Rab10 expression at DIV14 (Figure 1A). Previous studies have shown that Rab10 regulates neuronal outgrowth (Fukuda, 2008; Hutagalung and Novick, 2011). Consistent with these findings, we observed a significantly reduced dendrite and axon length in neurons infected with shRNA#9 at DIV0 (Figure 1B-D, 1G).

To test the effects of Rab10 depletion on synaptogenesis, synaptic vesicles (SVs) were quantified using the endogenous marker synaptophysin-1 (Syp1). Syp1 staining exhibited a punctate distribution at DIV14, indicating the accumulation of SVs in boutons/synapses, and no changes in the number of puncta per μm neurite or the intensity of Syp1 puncta (Figure 1E-F). These data confirm that Rab10 regulates neurite outgrowth, but we found no evidence for a role in synaptogenesis.

To test whether Rab10 depletion affects SV exocytosis, hippocampal neurons were infected with the SV exocytosis reporter Synaptophysin-pHluorin (SypHy; Figure 1H; Granseth et al., 2006). SV exocytosis was triggered by high-frequency electrical stimulation (HFS, 5s 40-Hz). The total vesicle pool was measured by briefly superfusing Tyrode's solution containing 50 mM NH_4Cl. The fraction of fused SVs, determined by the ratio of SypHy intensity upon HFS to the maximum intensity upon NH_4Cl superfusion, was comparable in the two groups (Figure 1I-J). In addition, SV endocytosis, measured by the fluorescence decay of SypHy after HFS, was unaffected by Rab10 depletion (Figure 1K). Therefore, we conclude that Rab10 is dispensable for SV exocytosis under intense stimulation.

Rab10 is a major regulator of DCV exocytosis.

To investigate the role of Rab10 in neuropeptide release, we depleted Rab10 levels at DIV0, expressed the DCV exocytosis reporter NPY-pHluorin at DIV9-10, and performed live-cell

127 imaging at DIV14. Our previous studies have demonstrated that NPY-pHluorin almost
128 exclusively localizes to DCVs as indicated by its strong co-localization with endogenous
129 markers of DCVs, such as BDNF and the chromogranins CHGA and CHGB (Arora et al.,
130 2017; Dominguez et al., 2018; Persoon et al., 2019). To achieve single-vesicle resolution
131 analysis of DCV exocytosis, we used single cultured hippocampal neurons on glial micro-
132 islands. Neurons were stimulated by 16 trains of 50 action potentials (APs) at 50 Hz, a
133 protocol known to trigger robust DCV exocytosis (Balkowiec and Katz, 2002; Emperador-
134 Melero et al., 2018; Gärtner and Staiger, 2002; Hartmann et al., 2001; Moro et al., 2021;
135 Persoon et al., 2019). Fusion events were detected as a rapid appearance of fluorescent puncta
136 (Figure 2—figure supplement 1A-B). DCV exocytosis in Rab10 KD neurons was
137 significantly reduced by 60% compared to control neurons (Figure 2—figure supplement 1C-
138 D). Furthermore, the total number of DCVs was reduced by 30% in Rab10 KD neurons
139 (Figure 2—figure supplement 1E). The fusion fraction, which represents the number of DCV
140 fusion events relative to the remaining DCV pool after stimulation, was also significantly
141 decreased by 50% in Rab10 KD neurons (Figure 2—figure supplement 1F). Overexpression
142 of wild-type, knockdown-resistant Rab10 rescued DCV exocytosis deficits in Rab10 KD
143 neurons (Figure 2—figure supplement 1C-F).
144
145 To overcome the potential confounding effects of impaired neurite outgrowth (Figure 1) and
146 reduced total DCV pool (Figure 2—figure supplement 1) upon Rab10 depletion starting at
147 DIV0, we adopted a more acute approach to interfere with Rab10 function, and late enough
148 not to affect neuronal morphology and the total DCV pool. Neurons were transfected with
149 shRNA against Rab10 at DIV7, fixed at DIV14, and stained with markers for dendrites
150 (MAP2), axons (SMI312), and SVs (Syp1). Rab10 expression was reduced by 70% after 7
151 days of infection (Appendix 1—figure 3). No significant alterations in total dendrite length,
152 axon length (Figure 2A-C, 2E), or synapse density (Figure 2D) were observed in Rab10 KD
153 neurons under these conditions. Therefore, to eliminate confounding effects on
154 morphological parameters, we reevaluated DCV exocytosis and all further experiments in
155 neurons infected with shRNA at DIV7. DCV exocytosis in Rab10 KD neurons remained
156 significantly lower by 50% compared to control neurons (Figure 2F-I). The fusion fraction
157 was also significantly reduced by 65% in Rab10 KD neurons (Figure 2K). Overexpression of
158 wild-type Rab10 rescued DCV exocytosis deficits. No significant differences in the total
159 number of DCVs (Figure 2J), DCV transport (Figure 2—figure supplement 2A-2B, 2E), or
160 cargo loading (Figure 2—figure supplement 2F-K) were observed. Moreover, only 10% of

161 DCVs co-transport with Rab10 (Figure 2—figure supplement 3). Thus, these data indicate
162 that Rab10 depletion specifically inhibits activity-dependent neuropeptide release in
163 hippocampal neurons, without effects on DCV biogenesis, cargo loading, and transport and
164 independent of Rab10's established role in neuronal outgrowth.
165
166 **Proteins involved in synaptic transmission and translation are severely dysregulated**
167 **upon Rab10 depletion.**
168 To comprehensively investigate Rab10 function in mature neurons, mass spectrometry
169 proteomics was performed on Rab10 KD and control neurons at DIV14. A total of
170 approximately 5400 unique proteins were identified and quantified in two biological
171 replicates. The complete list of proteins quantified in this study is presented in Appendix 1-
172 figure 3. Only differentially expressed proteins detected with high confidence characterized
173 by a log2(fold change) > 0.56, and q-value < 0.01, were included in the subsequent analysis.
174 Among the dysregulated proteins, 71% were upregulated, while 29% were downregulated,
175 resulting in a significant dysregulation of 19% of the total protein pool in Rab10 KD neurons.
176 These data indicate that Rab10 depletion leads to major neuronal proteome dysregulation
177 within 7 days after initiating knockdown (Figure 3A).
178
179 To gain insights into the functional consequences of Rab10 depletion, we performed Gene
180 Ontology (GO) analysis using ClueGO (Bindea et al., 2009). This analysis revealed that
181 biological processes related to chemical synaptic transmission were notably affected by
182 Rab10 depletion (Figure 3B). In addition, several biological processes related to protein
183 synthesis, such as cytoplasmic translation and ribosomal large subunit biogenesis, were
184 among the top 5 terms with the lowest *p*-values (Figure 3B). Subcellular localization analysis
185 of these dysregulated proteins upon Rab10 depletion showed that cytosolic ribosomal
186 proteins were the most significantly affected, followed by dendritic proteins (Figure 3C).
187 Further characterization of the dysregulated synaptic proteins was performed using SynGO
188 (Koopmans et al., 2019). Among the 391 significantly dysregulated proteins annotated in
189 SynGO, 205 were classified as presynaptic proteins and 237 as postsynaptic proteins. GO
190 enrichment analysis revealed that biological processes in metabolism were most dysregulated
191 upon Rab10 depletion. Among them, both pre and postsynaptic translation were significantly
192 dysregulated (Figure 3D). Consistent with the ClueGO analysis, SynGO highlighted a
193 significant dysregulation of presynaptic (34 of 391) and postsynaptic ribosomal proteins (44
194 of 391), supporting the involvement of Rab10 in the regulation of neuronal protein synthesis

195 (Figure 3E). Interestingly, all dysregulated ribosomal proteins were upregulated upon Rab10
196 depletion, which contrasts with the mostly downregulated expression observed in the other
197 classes of proteins (such as synaptic and cytoskeletal proteins) (Figure 3F-G). Taken
198 together, GO analysis with both ClueGO and SynGO indicates a dysfunction of protein
199 translation in Rab10 KD neurons.
200
201 Loss of Rab10 expression has been associated with altered ER morphology in mouse
202 embryonic cells (Lv et al., 2015), which may explain the selective upregulation of proteins
203 involved in ribosome function in our proteomics data. Indeed, ER proteins were dysregulated
204 substantially upon Rab10 depletion. Specifically, several rough ER proteins showed
205 differential regulation, with SEC61A1 being upregulated, SEC61G being downregulated, and
206 CLIMP remaining unchanged (Figure 3H). Most tubular ER proteins, such as RTN3/4 and
207 VAPB, were robustly decreased. Interestingly, one of the ER membrane Ca^{2+} channels,
208 SERCA2, showed a 50% reduction upon Rab10 depletion (Figure 3H).
209
210 Taken together, these analyses reveal that Rab10 depletion leads to major changes in protein
211 expression, especially synaptic and ribosomal proteins, the latter all upregulated in Rab10-
212 depleted neurons which suggests that protein synthesis is dysregulated, potentially due to
213 altered ER function.
214
215 **Rab10 regulates ER morphology and ribosomal protein levels.**
216 Given the substantial dysregulation of synapse and ribosome/ER proteins, we investigated
217 synapses and ER further using electron microscopy (Figure 4). These analyses revealed an
218 apparently normal synapse morphology in Rab10 depleted neurons with many SVs clustered
219 at the active zone, while DCVs were sparsely distributed along neurites and near the active
220 zone (Figure 4A). The length of the active zone (AZ) and postsynaptic density (PSD) were
221 both decreased by 10% upon Rab10 depletion (Figure 4C-D). However, other parameters of
222 synaptic ultrastructure, such as the diameter of SVs or DCVs, and the number of SVs per
223 synapse, were unchanged in Rab10 KD neurons (Figure 4E-H). Hence, despite substantial
224 dysregulation of synaptic proteins, overall synapse morphology was hardly affected.
225
226 Tubular ER was also observed in some presynaptic sections, consistent with previous studies
227 (Deng et al., 2021; Droz et al., 1975; Wu et al., 2017). The percentage of synaptic sections
228 containing tubular ER was decreased by 24% (37% in Control versus 28% in Rab10 KD).

229 Rough ER (rER) was also studied in the somata of Rab10 depleted and control neurons
230 (Figure 4I). The diameter of rER tubes was reduced by 15% in Rab10 KD neurons. Hence,
231 the substantial dysregulation of ribosomal and ER proteins in Rab10-depleted neurons was
232 accompanied by changes in the abundance of synaptic ER and small changes in ER
233 morphology in the soma.
234
235 To study these effects on ER abundance and morphology further, we performed
236 immunofluorescence staining for two endogenous ER markers, KDEL and RTN4. The
237 average fluorescence intensity of RTN4 and KDEL staining was significantly decreased by
238 35% and 25% respectively in Rab10 KD neurons (Figure 4—figure supplement 1A-C). The
239 relative distributions of RTN4 and KDEL in neurites, as calculated by the intensity ratio of
240 these two proteins in neurites over their somatic intensity, were reduced by 25% and 13%,
241 respectively (Figure 4—figure supplement 1D-E). In conclusion, the ultrastructural changes
242 in ER abundance and morphology upon Rab10 depletion were accompanied by altered
243 distribution of axonal ER, without affecting the ultrastructure of SVs and DCVs.
244
245 Finally, given the dynamic nature of ER tubular networks and the involvement of Rab10 in
246 ER tubule extension in COS- 7 cells (English and Voeltz, 2013), we tested ER dynamics in
247 Rab10 KD and control neurons expressing the luminal ER marker mCherry-ER3 using live-
248 cell imaging at DIV8, and performed FRAP experiments at DIV14. The recovery of
249 mCherry-ER3 intensity after photobleaching was significantly slower in Rab10 KD neurons
250 with only 50% recovery within three minutes, compared to 80% recovery in control neurons
251 (Figure 4—figure supplement 2C). Collectively, these data indicate that Rab10 depletion
252 leads to reduced levels of ER-resident proteins altered ER abundance and morphology, and
253 impaired ER dynamics.
254
255 **Rab10 regulates SERCA2 levels and ER Ca^{2+} homeostasis.**
256 The ER is the largest internal Ca^{2+} source in neurons and plays a crucial role in maintaining
257 neuronal Ca^{2+} homeostasis (Karagas and Venkatachalam, 2019). The maintenance of ER
258 Ca^{2+} primarily relies on the Sarco Endoplasmic Reticulum Calcium ATPase (SERCA), a Ca^{2+}
259 pump. Among the three major paralogs of SERCA, SERCA2 is particularly enriched in
260 neurons (Britzolaki et al., 2018; Periasamy and Kalyanasundaram, 2007; Xu and Van
261 Remmen, 2021). Consistent with the proteomic analysis which revealed a reduced SERCA2
262 expression upon Rab10 depletion (Figure 3), immunoblotting confirmed the reduction of

263 SERCA2 levels, showing a 50% reduction in Rab10 KD neurons (Figure 5A-5B). Therefore,
264 ER alternations in Rab10 KD neurons may disrupt Ca^{2+} homeostasis, which is essential for
265 DCV exocytosis.
266
267 To test this, we next measured the Ca^{2+} concentration in ER ($[Ca^{2+}]_{ER}$) using the ER Ca^{2+}
268 indicator ER-GCaMP6 (de Juan-Sanz et al., 2017). We observed a reduction in $[Ca^{2+}]_{ER}$ in
269 soma from 130 μM in control neurons to about 70 μM in Rab10-depleted neurons (Figure
270 5C). $[Ca^{2+}]_{ER}$ in neuritis was also reduced by 15% in Rab10 KD neurons (Figure 5D). The
271 reduction of $[Ca^{2+}]_{ER}$ was rescued by the expression of a knockdown-resistant Rab10
272 construct. To validate this observation, we assessed ER Ca^{2+} homeostasis indirectly by
273 measuring the effect of caffeine on cytosolic Ca^{2+} concentration. As expected, in the absence
274 of extracellular Ca^{2+}, caffeine application (1 μM) triggered an increase in cytosolic Ca^{2+} due
275 to Ca^{2+} release from the ER in both wild-type and Rab10 depleted neurons. However, the
276 peak and the area of the caffeine-induced Ca^{2+} response curves were both reduced by 30% in
277 Rab10 KD neurons (Figure 5—figure supplement 1).
278
279 Furthermore, we examined ER Ca^{2+} dynamics following a 10-minute caffeine treatment.
280 Caffeine activates the ryanodine receptor (RyR), leading to the depletion of ER Ca^{2+} (Endo,
281 1975; Fujimoto et al., 1980). As expected, perfusion with caffeine-induced ER
282 Ca^{2+} depletion, followed by recovery towards pre-stimulation levels (Figure 5F-G). In wild-
283 type neurons, Ca^{2+} levels were recovered by 90% at T=190 s. However, the refilling of ER
284 Ca2+ was significantly delayed in Rab10 KD neurons or GDP-Rab10 expressing neurons.
285 Ca2+ levels were only recovered by 50% at T=190 s (Figure 5G-H) in these neurons.
286
287 Finally, to investigate the consequence of the ER Ca^{2+} depletion on neuronal Ca^{2+}
288 homeostasis in Rab10 KD neurons, we measured cytosolic Ca^{2+} responses triggered by action
289 potentials (AP) using the Ca^{2+} indicator Fluo5F (Figure 6A-C) and the genetically encoded
290 Synaptophysin-GCaMP6 (Figure 6D-F). The AP-induced Ca^{2+} responses in the soma, as
291 measured by Fluo5F, were reduced by 40% upon Rab10 depletion (Figure 6C). Similarly, the
292 AP-induced Ca^{2+} responses in presynaptic nerve terminals, measured by Synaptophysin-
293 GCaMP6, were also reduced (20%, Figure 6F), although this effect was smaller than the
294 effects of Rab10 KD on ER Ca^{2+} levels and Caffeine-induced ER Ca^{2+} depletion (Figure 5).
295 Taken together, these data suggest that Rab10 knockdown leads to ER Ca^{2+} depletion and
296 impairs neuronal Ca^{2+} homeostasis, which may be attributed to the reduced levels of

297 SERCA2 level and slower ER Ca^{2+} refilling and may contribute to the impaired DCV
298 exocytosis.
299
300 **Rab10 depletion impairs ionomycin-induced DCV exocytosis.**
301 To determine whether the impaired Ca^{2+} signaling explains the DCV exocytosis deficiency in
302 Rab10 KD neurons, we stimulated DCV exocytosis using the Ca^{2+} ionophore ionomycin.
303 This approach bypasses cellular Ca^{2+} homeostasis and artificially increases the intracellular
304 Ca^{2+} concentration enough to trigger DCV exocytosis (Persoon et al., 2019). Unexpectedly,
305 DCV exocytosis was still reduced in Rab10 KD neurons (Figure 7A-B). Although the
306 reduction was substantial, 45%, this impairment was not as substantial as observed for action
307 potential-induced DCV exocytosis (65%, Figure 2K). The total number of DCV was nearly
308 identical between control and Rab10 KD neurons (Figure 7D). Thus, although a minor
309 fraction of the DCV exocytosis deficits may be explained by impaired Ca^{2+} signaling
310 (difference between 45% and 65%), other deficits explain most of the DCV exocytosis
311 deficiency in Rab10 KD neurons.
312
313 **Rab10 regulates neuronal protein synthesis.**
314 Since significant dysregulation of ER markers and ribosomal proteins was observed upon
315 Rab10 depletion, we investigated the effects of Rab10 on protein synthesis using SUnSET to
316 detect nascent peptides formed during puromycin pulse labeling (Schmidt et al., 2009).
317 SUnSET analysis revealed that global protein synthesis was reduced by 30% upon Rab10
318 depletion (Figure 8A-B).
319
320 Protein synthesis impairments may be rescued by supplementation with leucine, a branched-
321 chain amino acid, that promotes protein synthesis by activating the mTOR pathway
322 (Ananieva et al., 2016). To test this in Rab10 KD neurons, additional L-leucine was added to
323 the culture medium to increase the concentration to 5 mM for three days. Indeed, 5mM
324 leucine supplementation significantly restored global protein synthesis deficits caused by
325 Rab10 depletion (Figure 8A-B).
326
327 Finally, a similar impairment in global protein synthesis was observed when a loss-of-
328 function mutant of Rab10 (Rab10T23N) was overexpressed in wild-type neurons (Figure 8A-
329 B). The deficit in protein translation is unlikely attributable to the upregulated mTORC1
330 signaling as the relative phosphorylation level of pS6K1 was unaffected in Rab10 KD

331 neurons (figure 8-figure supplement 1). Thus, Rab10 depletion or Rab10T23N expression
332 reduces global protein synthesis in neurons, probably by dysregulation of ER and ribosomal
333 function.
334
335 **Leucine supplementation restores normal DCV exocytosis.**
336 We hypothesized that protein synthesis deficits in Rab10-depleted neurons explain most of
337 the impaired DCV exocytosis (in addition to a minor fraction explained by disturbed Ca^{2+}-
338 homeostasis, see above) and tested whether leucine supplementation could rescue the DCV
339 exocytosis deficits in Rab10 KD neurons. Rab10 depleted neurons expressing NPY-pHluorin
340 were treated with 5mM leucine three days before live-cell imaging, or with dimethyl
341 sulfoxide (DMSO) as a control. Leucine supplementation restored DCV exocytosis by 80%
342 caused by Rab10 depletion but did not alter DCV exocytosis in control neurons (Figure 8C-
343 F). However, leucine supplementation failed to rescue the defects in ER morphology in
344 Rab10 KD neurons (figure 8-figure supplement 2).
345
346 These results suggest that impaired protein synthesis is a major factor contributing to DCV
347 exocytosis deficits in Rab10-depleted neurons.
348
349 ## Discussion
350 In this study, we investigated the function of Rab10 in neuropeptide release in mature mouse
351 hippocampal neurons. We found that DCV exocytosis triggered by action potential trains was
352 reduced by 65% upon Rab10 depletion, whereas SV exocytosis was unaffected. In addition,
353 we observed a depleted ER Ca^{2+} pool and an impaired action potential-induced Ca^{2+} response
354 in Rab10 KD neurons. However, DCV exocytosis triggered by Ca^{2+}-ionophore ionomycin, a
355 triggering method independent of Ca^{2+} channels and internal Ca^{2+}-stores, was also impaired,
356 albeit to a lesser extent. Furthermore, ribosomal proteins were massively dysregulated, and
357 protein synthesis was impeded upon Rab10 depletion. Finally, the DCV exocytosis deficit in
358 Rab10 KD neurons was largely rescued by leucine supplementation. We conclude that the
359 strong inhibition of DCV exocytosis upon Rab10 depletion is mostly due to protein synthesis
360 deficiency and to a lesser extent by dysregulation of Ca^{2+} channels or internal Ca^{2+}-stores.
361
362 **Rab10 regulates neurite outgrowth but not membrane homeostasis in mature neurons.**

363 Rab10 is highly enriched in neurons and plays crucial roles in neuronal development (Taylor
364 et al., 2015; Wang et al., 2011; Xu et al., 2014). Consistent with these previous findings, we
365 observed a reduction of axonal and dendritic outgrowth in Rab10-depleted neurons. Also
366 consistent with previous findings in invertebrates (Sasidharan et al., 2012), we observed that
367 the endogenous levels of SV markers are unchanged, indicating that SV biogenesis was
368 unaffected. However, morphological characterization of neurons infected with shRNAs after
369 the first week in culture did not identify changes in the total length of dendrites or axons,
370 indicating that membrane homeostasis in mature neurons was unaffected by Rab10
371 knockdown. Therefore, the strong deficit in neuropeptide release in DIV7-infected neurons is
372 unlikely to be confounded by Rab10-dependent aspects of neuronal development.
373
374 **Rab10 is crucial for DCV exocytosis.**
375 In *C. elegans*, neuropeptide release was abolished in Rab10 deletion mutants (Sasidharan et
376 al., 2012). We observed a 60% reduction in neuropeptide release in Rab10-depleted mature
377 mouse hippocampal neurons. The difference in effect size could be explained by the
378 incomplete Rab10 depletion with shRNA silencing or by redundant pathways in mammals,
379 e.g. Rab10 and Rab8 are closely related paralogs and share many common effectors (Homma
380 et al., 2020).
381
382 Unlike Rab3, which travels together DCVs and exhibits a reduction of over 90% in DCV
383 exocytosis in its quadruple knock-out neurons (Persoon et al., 2019), Rab10 does not
384 typically travel with DCVs (Figure 2—figure supplement 3). In addition, no changes in DCV
385 size, puncta intensity, puncta distribution, travel velocity, or distance were detected in Rab10
386 KD neurons. We conclude that DCV exocytosis deficiency in Rab10-depleted neurons is not
387 caused by alterations in DCV biogenesis or transport and that Rab10 is not required for DCV
388 trafficking.
389
390 Although Rab10 is found in subcellular fractions enriched in synaptic vesicles (Takamori et
391 al., 2006; Taoufiq et al., 2020), it is dispensable for SV exocytosis. Evoked postsynaptic
392 currents (EPSCs) were unaffected in Rab10 mutants in *C. elegans* (Sasidharan et al., 2012).
393 In line with this, SV exocytosis was unaffected in Rab10-depleted hippocampal neurons.
394 These results indicate that Rab10 is selectively required for DCV exocytosis, not for SV
395 exocytosis. Strikingly, many synaptic proteins, including many involved in SV exocytosis,
396 are among the most severely dysregulated proteins upon Rab10 depletion. SV exocytosis may

397 be more resilient to acute protein changes (Sinha et al., 2011) than DCVs. In addition, vesicle
398 secretion properties are different for DCVs and SVs. Unlike SVs, which are secreted upon a
399 single electrical stimulation, DCVs need prolonged or more intense stimulation for the
400 induction of fusion. Thus, the regulatory effects of Rab10 on DCV exocytosis might be
401 amplified under prolonged stimulation.
402
403 **Ca^{2+} homeostasis deficits contribute to DCV exocytosis deficits in Rab10 KD neurons.**
404 Rab10 KD neurons showed depleted ER Ca^{2+} and impaired cytosolic Ca^{2+} responses. These
405 effects may contribute to the observed DCV exocytosis deficits. Ca^{2+} released from the ER
406 promotes DCV mobility and potentiates neuropeptide release via activating the CaMKII
407 pathway in *Drosophila* (Shakiryanova et al., 2007). However, this might not be the case in
408 mouse neurons since most axonal ER takes Ca^{2+} up from cytosol, instead of releasing it (de
409 Juan-Sanz et al., 2017). Secondly, triggering Ca^{2+} release from the ER did not alter DCV
410 transport and fusion (unpublished data from our lab). Finally, a previous study from our lab
411 has shown that CaMKII deficiency does not alter DCV exocytosis (Moro et al., 2020).
412 Hence, dysregulation of ER Ca^{2+} dynamics may not directly explain the observed DCV
413 exocytosis deficits in Rab10-depleted neurons. However, ER Ca^{2+} also regulates Ca^{2+} influx
414 by modulating L-type voltage-gated Ca^{2+} channels at the plasma membrane via a STIM1-
415 based feedback loop (de Juan-Sanz et al., 2017). Given the importance of Ca^{2+} influx for
416 DCV exocytosis, dysregulation of ER Ca^{2+} dynamics may indirectly explain DCV exocytosis
417 deficiency upon Rab10 depletion. However, Ionomycin-triggered DCV exocytosis, which
418 bypasses voltage-gated Ca^{2+} channels, was still reduced, albeit to a lesser extent compared to
419 action potential trains. This difference in effect size is consistent with a limited contribution
420 for dysregulation of Ca^{2+} dynamics and voltage-gated Ca^{2+} channels to explain the impaired
421 DCV exocytosis in Rab10 KD neurons, while the majority of this phenotype is explained by
422 deficits downstream of protein synthesis.
423
424 **A role of Rab10 in protein synthesis largely explains DCV exocytosis deficiency in**
425 **Rab10 KD neurons.**
426 In line with the previous study (Lv et al., 2015), which indicated alteration in ER morphology
427 in Rab10 KO embryonic cells. We observed impaired ER morphology and upregulated
428 ribosomal proteins upon Rab10 depletion. The upregulation of ribosomal proteins might be a
429 compensatory response to altered ER structure as mutation of other ER-shaping proteins,
430 such as VCP and ALT1, causes similar ribosomal abnormalities as Rab10 depletion (Shih

431 and Hsueh, 2016). Protein homeostasis is vital for neuronal function and deficiency in protein
432 translation is related to several CNS disorders (Cajigas et al., 2010; Holt et al., 2019; Koga et
433 al., 2011; Laguesse and Ron, 2020).
434
435 Dysregulation of ribosomes and ER is probably sufficient to explain the impaired protein
436 translation in Rab10 KD neurons. Depleted ER Ca^{2+} may induce ER stress (Arruda and
437 Hotamisligil, 2015; Fu et al., 2011) which may also contribute to protein translation
438 inhibition, but ATF4 levels are unaffected in Rab10 KD neurons, suggesting that ER stress is
439 at best limited (Figure 4—figure supplement 3A-B). In addition, Rab10 regulates the
440 retrograde transport of TrkB signaling endosomes (Lazo and Schiavo, 2023), which may
441 activate the CREB/mTOR pathway and promote protein synthesis (Moya-Alvarado et al.,
442 2023). Hence, impaired TrkB transport may also contribute to impaired protein translation in
443 addition to dysregulated ribosomes in Rab10 KD neurons. We found that restoring protein
444 synthesis with leucine efficiently increased protein synthesis and largely restored DCV
445 exocytosis deficiency in Rab10-depleted neurons. We conclude that dysregulation of protein
446 synthesis results in DCV exocytosis deficits in these neurons.
447
448 In conclusion, our data demonstrate the importance of Rab10 in neuropeptide release and ER
449 homeostasis. We observed altered ER morphology, reduced ER Ca^{2+} concentration, impaired
450 protein synthesis, and impaired neuropeptide release in Rab10-depleted neurons. These
451 observations shed light on the pathogenesis of Rab10-related disease. In addition, we have
452 shown leucine can largely rescue deficiency in protein synthesis and neuropeptide release in
453 Rab10-depleted neurons, providing a potential treatment for disorders associated with
454 neuropeptide abnormalities such as depression and anxiety.
455

456 **Contributions**

457 Conceptualization: JD, RT, MV
458 Methodology: JD, MC, RD, JW, KWL, ABS, RT, MV
459 Investigation: JD, RT, MV
460 Visualization: JD, MC, KWL, JW, RT, MV
461 Funding acquisition: RT, MV
462 Supervision: RT, MV
463 Writing – original draft: JD, RT, MV

Acknowledgment

This work was supported by a European Research Council (ERC) Advanced grant (322966) of the European Union (to MV), COSYN (Comorbidity and Synapse Biology in Clinically Overlapping Psychiatric Disorders, Horizon 2020 Program of the European Union under RIA grant agreement 667301, to MV) and the JPND Neuron Cofund ERA-Net SNAREopathy (to RFT). We thank Rien Dekker for the electron microscopy data, Robbert Zalm and Ingrid Saarloos for cloning and producing viral particles, Joke Wortel for the animal breeding, Lisa Laan and Desiree Schut for glia and primary neuron culture assistance, Jurjen Broeke for technical support, and members of the DCV team for discussions and input. The authors declare no competing interests. Correspondence should be addressed to Matthijs Verhage at matthijs@cncr.vu.nl.

476 **Figures and figure legends**

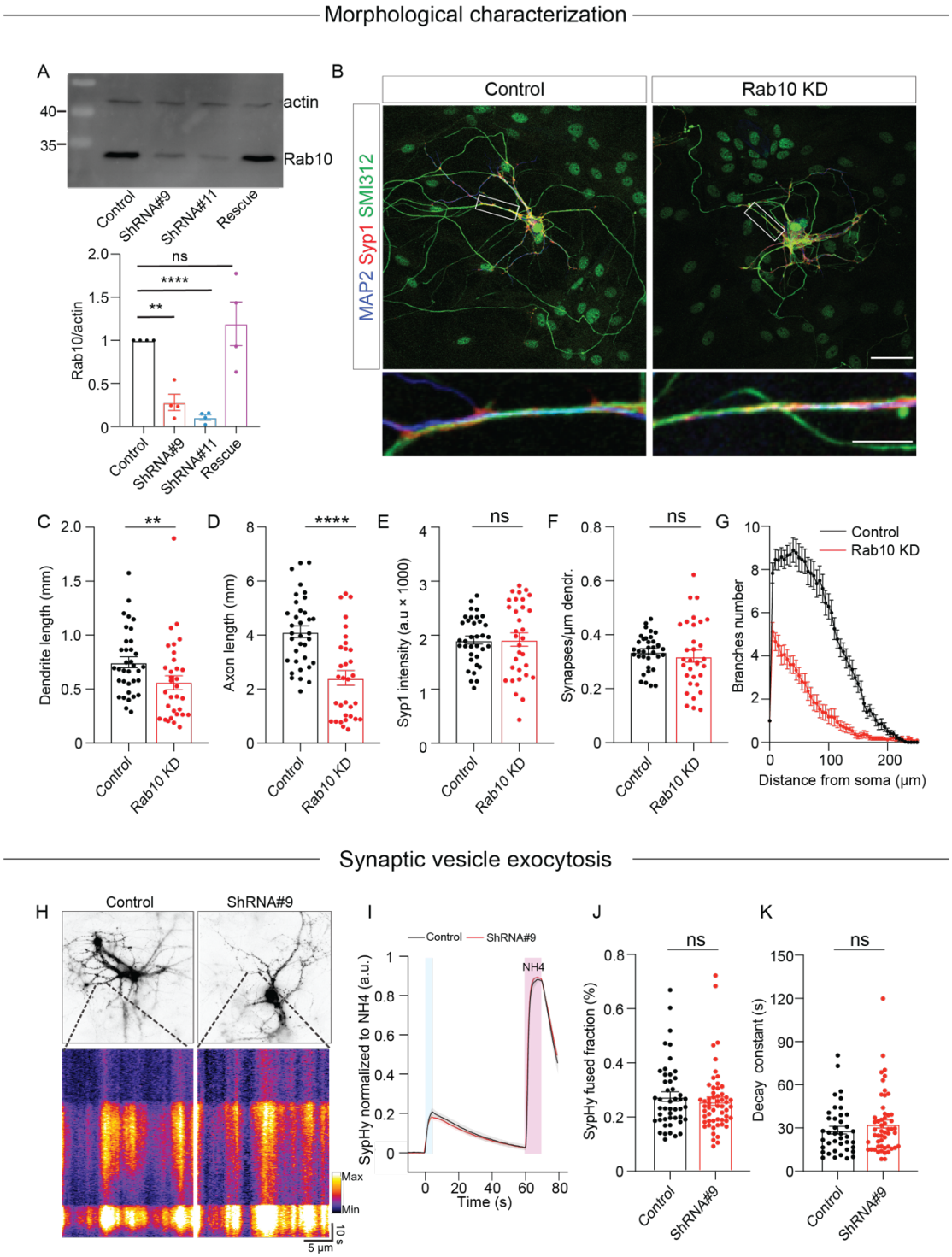

477

478 **Figure 1: Rab10 is required for neuronal outgrowth but dispensable for SV exocytosis**
479 **evoked by intense stimulations.**

480 (A) Representative immunoblotting showing knockdown and rescue of Rab10 expression in
481 cultured primary neurons infected with shRNA against Rab10 or rescue constructs (upper)
482 and quantification of Rab10 levels (bottom).

483 (B) Example images of control or Rab10 KD hippocampal neurons (DIV14) stained for the
484 dendrite marker MAP2 (blue), the synapse marker Syp1 (red), and the axonal marker SMI312
485 (green). Scale bar: 50 µm (upper) and 10 µm (bottom).
486 (C) Quantification of the dendritic length (MAP2).
487 (D) Quantification of the axonal length (SMI312).
488 (E) Quantification of Syp1 intensity per synapse per neuron.
489 (F) Quantification of the Syp1-positive synapse density in MAP2-positive dendrites.
490 (G) Sholl analysis showing the mean number of dendritic branches against the distance from the
491 soma.
492 (H) Example neurons infected with the SV fusion marker SypHy (upper), typical kymographs of
493 neurites showing SypHy intensity increase during stimulation and upon NH_4Cl superfusion
494 (bottom).
495 (I) The average signal SypHy from active synapses, normalized from baseline to maximum
496 fluorescence upon NH_4Cl superfusion.
497 (J) SV exocytosis determined as the ratio of the maximum SypHy intensity during stimulation to
498 the maximum during NH_4Cl stimulation.
499 (K) SV endocytosis determined as the SypHy signal decay time constant τ in the 60 s after field
500 stimulation.
501 All Data are plotted as mean±s.e.m. (A) N = 4, n = 4, one sample t-test. (C-G) Control: N = 3, n = 35;
502 ShRNA#9: N = 3, n = 32. (J, K) Control: N = 3, n = 56; ShRNA#9: N = 3, n = 56. (C-F, J, K) A one-
503 way ANOVA tested the significance of adding experimental group as a predictor . **** = $p<0.0001$,
504 ** = $p<0.01$, ns = not significant.

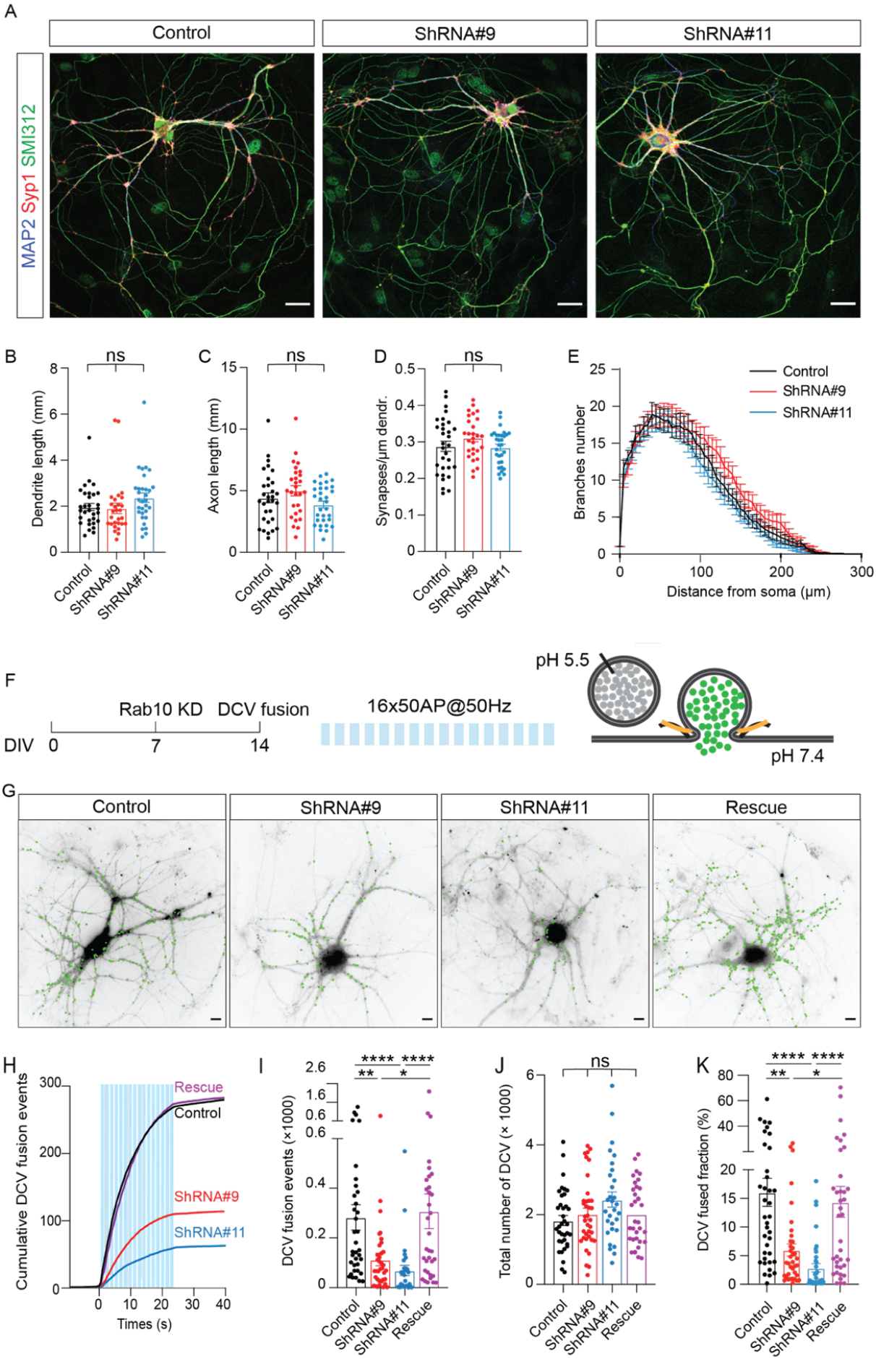
A
Control
ShRNA#9
ShRNA#11
MAP2 Syp1 SMI312
B
ns
Dendrite length (mm)
Control
ShRNA#9
ShRNA#11
C
ns
Axon length (mm)
D
ns
Synapses/µm dendr.
E
Control
ShRNA#9
ShRNA#11
Branches number
Distance from soma (µm)
F
Rab10 KD
DCV fusion
16x50AP@50Hz
DIV 0
7
14
pH 5.5
pH 7.4
G
Control
ShRNA#9
ShRNA#11
Rescue
H
Rescue
Control
ShRNA#9
ShRNA#11
Cumulative DCV fusion events
Times (s)
I
DCV fusion events (×1000)
Control
ShRNA#9
ShRNA#11
Rescue
J
ns
Total number of DCV (× 1000)
K
DCV fused fraction (%)

505

506 **Figure 2: Rab10 is a major regulator of DCV exocytosis.**

507 (A) Example images of control and Rab10 KD hippocampal neurons (DIV14) stained for MAP2
508 (blue), Syp1 (red) and SMI312 (green). Scale bar: 30 µm.
509 (B) Quantification of the dendritic length (MAP2).
510 (C) Quantification of the axonal length (SMI312).
511 (D) Quantification of the Syp1-positive synapse density in MAP2-positive dendrites.
512 (E) Sholl analysis showing the mean number of dendritic branches against the distance from the
513 soma.
514 (F) Schematic representation of DCV fusion assay. DCVs are labeled with NPY-pHluorin, and
515 neurons are stimulated with one train of 16 bursts of 50 APs at 50 Hz (light blue bars).
516 (G) Representative neurons during electrical stimulation superimposed with NPY-pHluorin fusion
517 events (green dots). Scale bar: 5 µm.
518 (H) Cumulative plot of DCV fusion events per cell. Light blue bars represent the stimulation
519 trains.
520 (I) Summary graph of DCV fusion events per cell.
521 (J) The total number of DCVs (total pool) of neurons analyzed in Figure 2H, measured as the
522 number of NPY-pHluorin puncta upon NH_4Cl perfusion.
523 (K) Fraction of NPY-pHluorin-labeled DCV fusing during stimulation.
524

525 All Data are plotted as mean±s.e.m. (B-D) Control: N = 3, n = 31; ShRNA#9: N = 3, N = 28;
526 ShRNA#11: N = 3, n = 31. (I-K) Control: N = 4, n = 36; shRNA#9: N = 4, N = 37; shRNA#11: N =
527 4, n = 30; Rescue: N = 4, n = 34. A one-way ANOVA tested the significance of adding experimental
528 group as a predictor. **** = $p<0.0001$, *** = $p<0.001$, ** = $p<0.01$, * = $p<0.05$, ns = not significant.

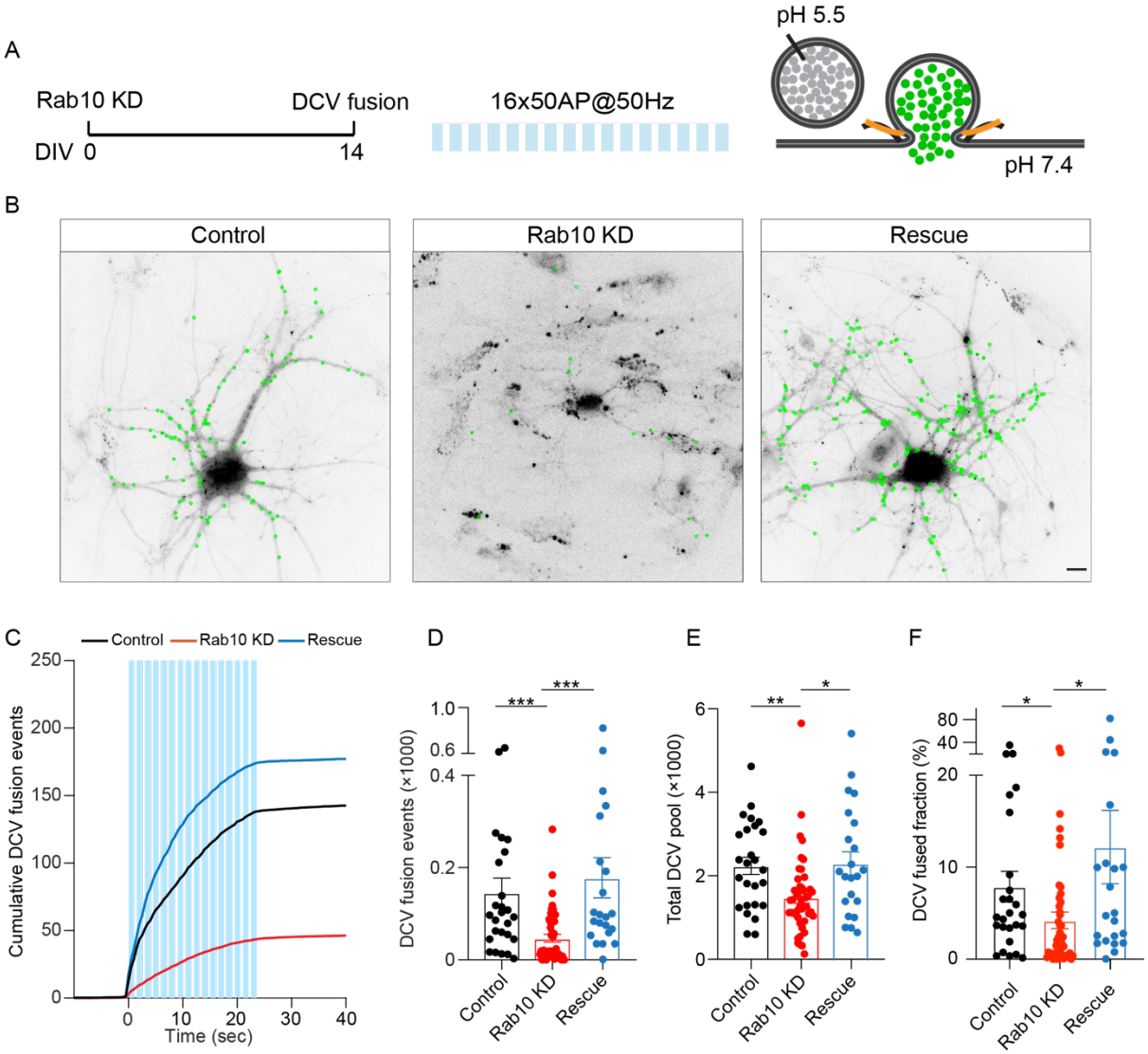

Figure 2—figure supplement 1: Rab10 depletion at DIV0 impedes DCV fusion.

(A) Schematic representation of DCV fusion assay. DCVs are labeled with NPY-pHluorin, and neurons are stimulated with one train of 16 bursts of 50 APs at 50 Hz (light blue bars).

(B) Representative neurons during electrode stimulation superimposed with NPY-pHluorin fusion events (green dots). Scale bar: 10 µm.

(C) Cumulative plot of DCV fusion events per cell.

(D) Summary graph of DCV fusion events per cell.

(E) Total number of DCVs (total pool) of neurons, measured as the number of NPY-pHluorin puncta upon NH_4Cl perfusion.

(F) Fraction of NPY-pHluorin-labeled DCV fusing during stimulation.

All Data are plotted as mean±s.e.m. (D-F) Control: N = 3, n = 26; Rab10 KD: N = 3, n = 47; Rescue: N = 3, n = 22. (D-F) A one-way ANOVA tested the significance of adding experimental group as a predictor. *** = p<0.001, ** = p<0.01, * = p <0.05.

DCV transport

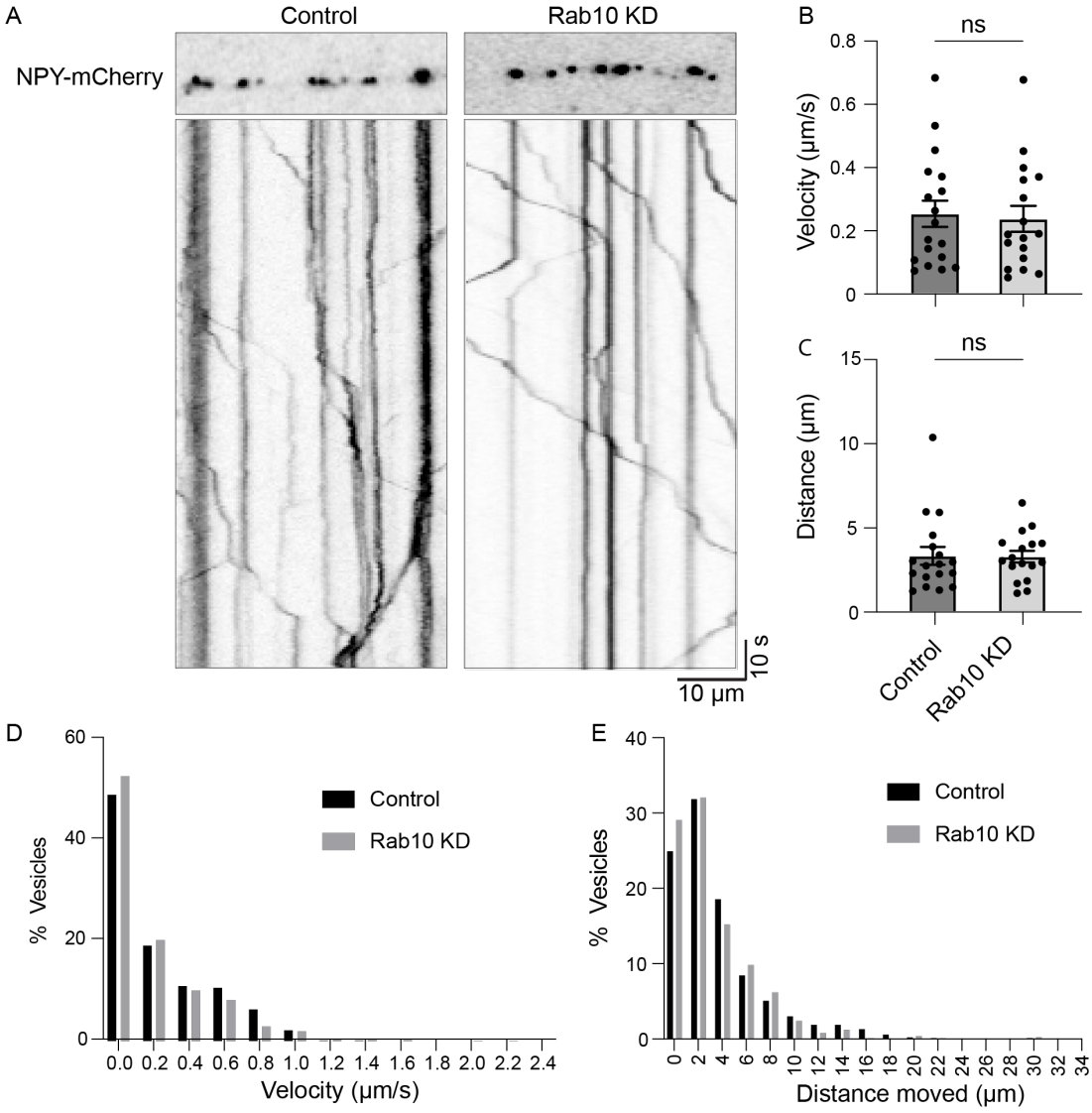

NPY-pHluorin properties

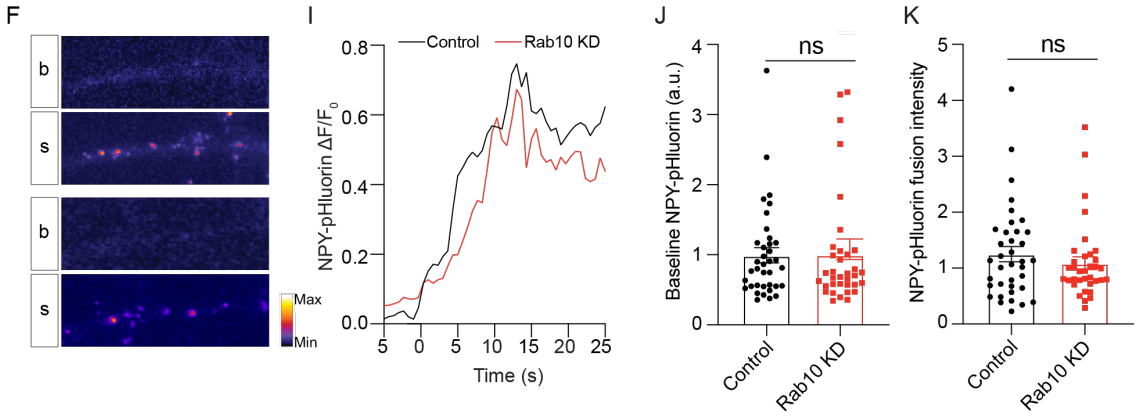

543

544 **Figure 2—figure supplement 2: Rab10 depletion does not affect DCV transport or**
545 **cargo loading.**
546 (A) Representative kymographs illustrating the transport of NPY-mCherry labeled DCVs in
547 control and Rab10 KD neurons.
548 (B) Quantification of average velocity (µm/s) of control and Rab10 KD neurons.
549 (C) Quantification of average distance moved from the start (µm) of control and Rab10 KD
550 neurons.
551 (D) Histogram of average velocity (µm/s) of control and Rab10 KD neurons.
552 (E) Histogram of average distance moved from the start (µm) of control and Rab10 KD neurons.
553 (F) Typical neurite expressing NPY-pHluorin during baseline (b), and during stimulation (s).
554 (G) Average traces of NPY-pHluorin fusion events aligned at the moment of fusion (0 seconds).
555 (H) Quantification of NPY-pHluorin baseline fluorescence before stimulation.
556 (I) Quantification of average NPY-pHluorin fusion intensity per cell.
557 All Data are plotted as mean±s.e.m. (B, C) Control: N = 3, n = 18; Rab10 KD: N = 3, n = 17. (H, I)
558 Control: N = 3, n = 37; Rab10 KD: N = 3, n = 35. A one-way ANOVA tested the significance of
559 adding experimental group as a predictor. ns = not significant.
560

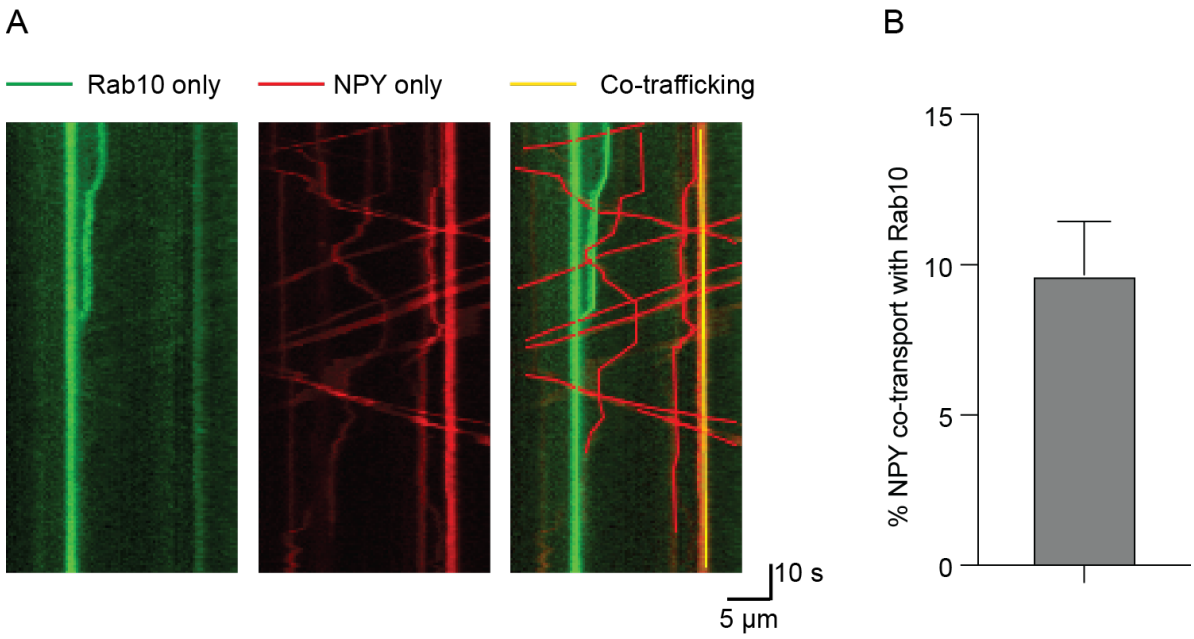

561
562 **Figure 2—figure supplement 3: Rab10 does not typically co-transport together with**
563 **DCVs.**
564 (A) Representative kymographs of neurons co-infected with Rab10-GFP and NPY-mCherry.
565 (B) Percentage moving DCVs that co-transport with Rab10. Data are plotted as mean±s.e.m (N =
566 3, n = 22).
567 Data are plotted as mean±s.e.m.

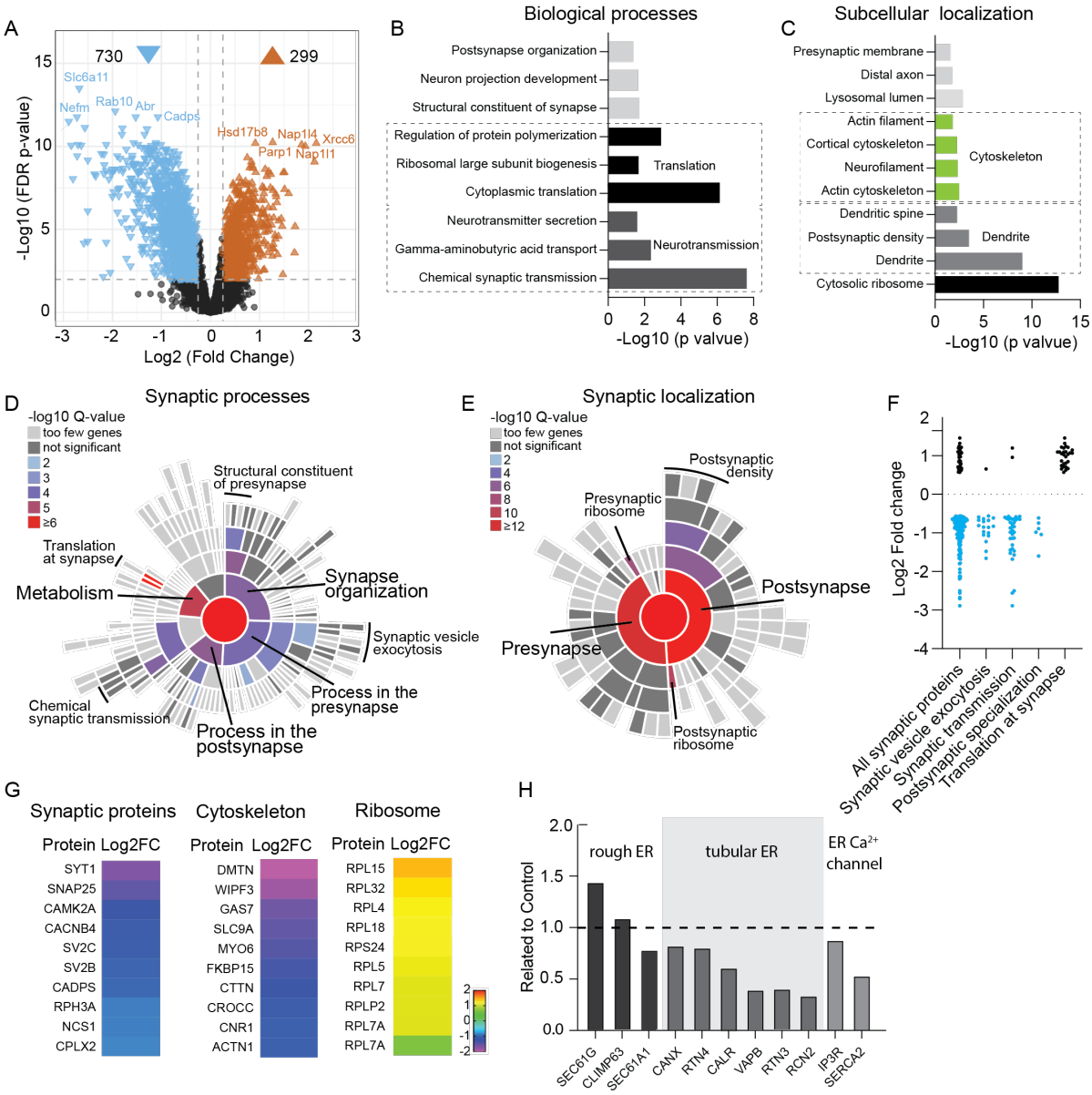

Figure 3: Depletion of Rab10 leads to dysregulation of proteins enriched in presynaptic transmission and cytosolic translation.

(A) Volcano plots showing significantly dysregulated proteins in Rab10 depleted neurons.

(B) GO enrichment analysis of functional pathways of the significant hits with ClueGO. Shown are the Bonferroni corrected p-values.

(C) GO enrichment analysis of subcellular localization of the significant hits with ClueGO. Shown are the Bonferroni corrected p-values.

(D) Sunburst plot showing the annotation in synaptic function of the altered proteins in Rab10 depleted neurons.

(E) Sunburst plot showing the annotation in synaptic location of the altered proteins in Rab10 depleted neurons.

580 (F) Log2 fold changes of synaptic proteins within SynGO terms. Downregulated proteins are
581 shown in blue and upregulated proteins are shown in black.
582 (G) Examples of proteins that are significantly affected by Rab10 depletion grouped by their
583 subcellular localization. Heat maps represent the degree of up- or downregulation.
584 (H) Selective MS data analysis of ER-related proteins in Rab10 KD neurons. Bars show the fold
585 change of the indicated peptides compared to the control.
586
587

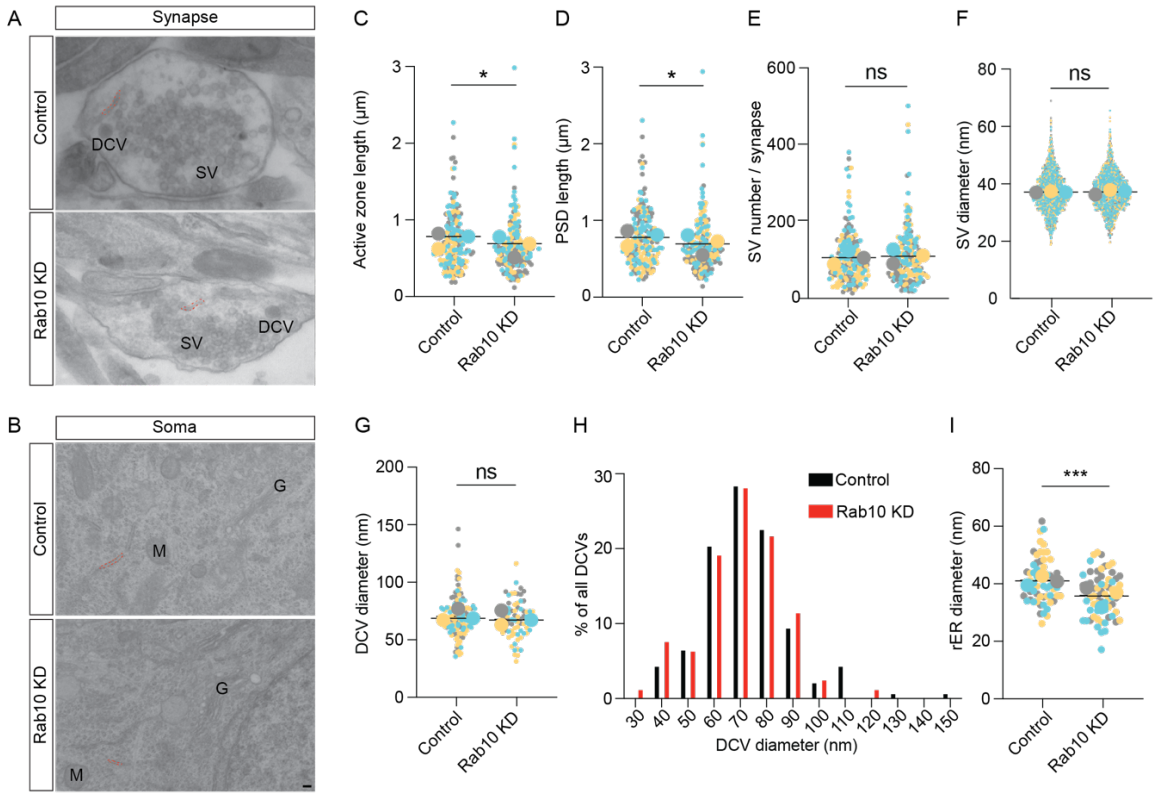

588
589 **Figure 4**: **Rab10 regulates synapse size and ER morphology.**
590 (A) Representative EM pictures showing the ultrastructure of synapses. Scale bar 100 nm.
591 Synaptic ER is indicated by red dotted lines.
592 (B) Representative EM pictures showing the ultrastructure of soma. Rough ER (rER) is indicated
593 by red dotted lines. M: mitochondrion, G: Golgi. Scale bar: 100 nm.
594 (C) Quantification of the length of active zone and postsynaptic density (PSD).
595 (D) Quantification of the length of postsynaptic density (PSD).
596 (E) Quantification of SV number per synapse and SV diameter.
597 (F) Quantification of SV diameter.
598 (G) Quantification of DCV diameter.
599 (H) Frequency distribution of DCVs by diameter.
600 (I) Quantification of the diameter of rough ER (rER).

601 Data are plotted with Superplot (Figure. 4C-G, I), where averages from three independent cultures are
602 shown as large circles and single observations are shown as dots. Horizontal lines represent the means
603 of the averages from three weeks. Data from different cultures are grouped with different colors. (C-
604 D) Control: N = 3, n = 184; shRNA#9: N = 3, n = 187. (E) Control: N = 3, n = 189; shRNA#9: N = 3,
605 n = 188. (F) Control: N = 3, n = 1770; shRNA#9: N = 3, n = 1803. (G) Control: N = 3, n = 137;
606 shRNA#9: N = 3, n = 122. (I) Control: N = 3, n = 63; shRNA#9: N = 3, n = 64. (C-G, I) linear mixed
607 model analysis. *** = p<0.001, * = p <0.05, ns = not significant.
608

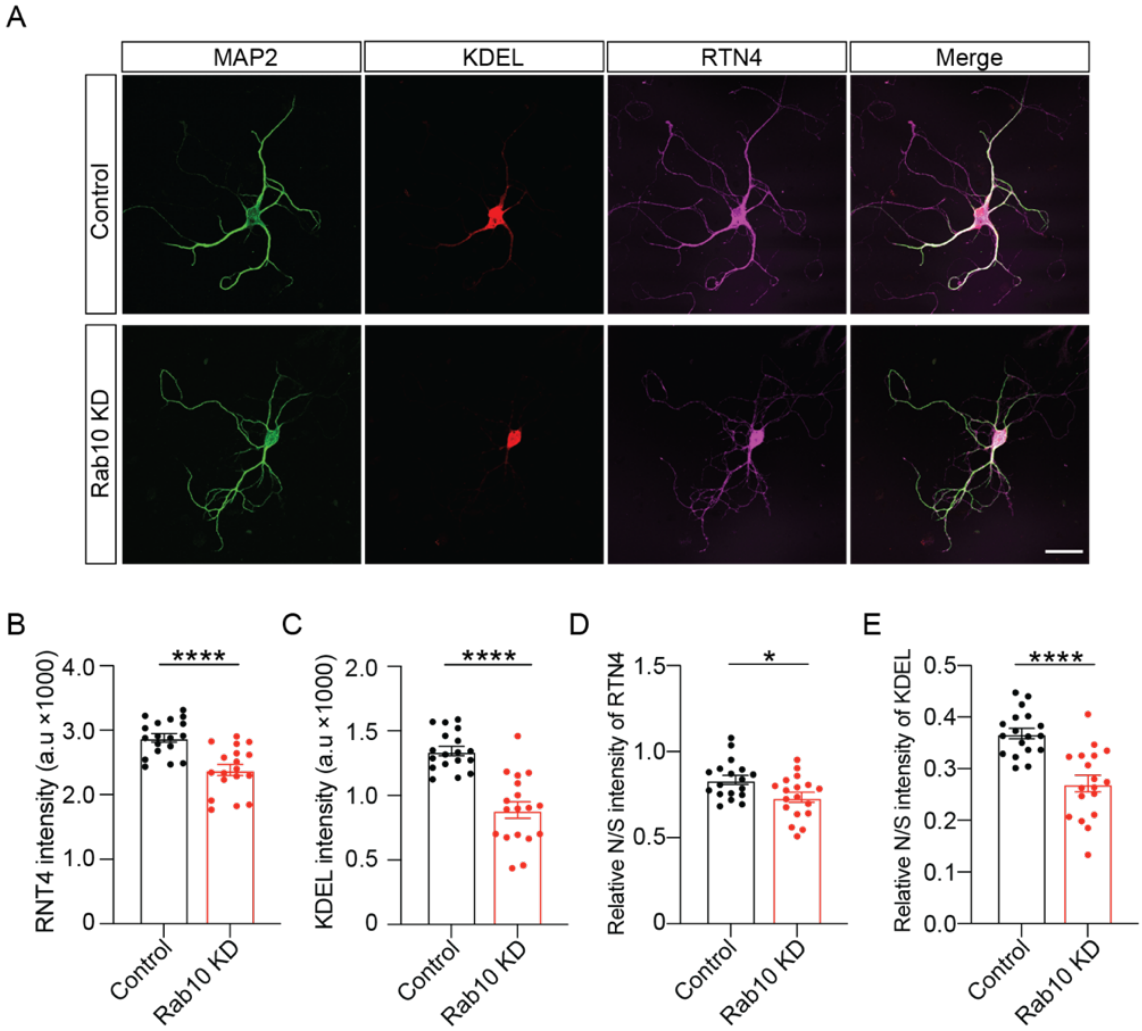

609

610 **Figure 4—figure supplement 1: Altered ER morphology in Rab10 KD neurons.**

611 (A) Example images of control or Rab10 KD hippocampal neurons (DIV14) stained for the
612 dendrite marker MAP2 (green), two ER markers KDEL (red) and RTN4 (magenta). Scale bar:
613 50 µm.

614 (B) Quantification of RTN4 intensity in MAP2-positive dendrites.

615 (C) Quantification of KDEL intensity in MAP2-positive dendrites.

616 (D) The ratio of neuritic to somatic RTN4 intensity (N/S).

617 (E) The ratio of neuritic to somatic KDEL intensity (N/S).

618 All Data are plotted as mean±s.e.m. (B-D) Control: N = 3, n = 18; Rab10 KD: N = 3, n = 18; (B-D) A
619 one-way ANOVA tested the significance of adding experimental group as a predictor. **** =
620 p<0.0001, *** = p<0.001, ** = p<0.01, * = p <0.05.
621

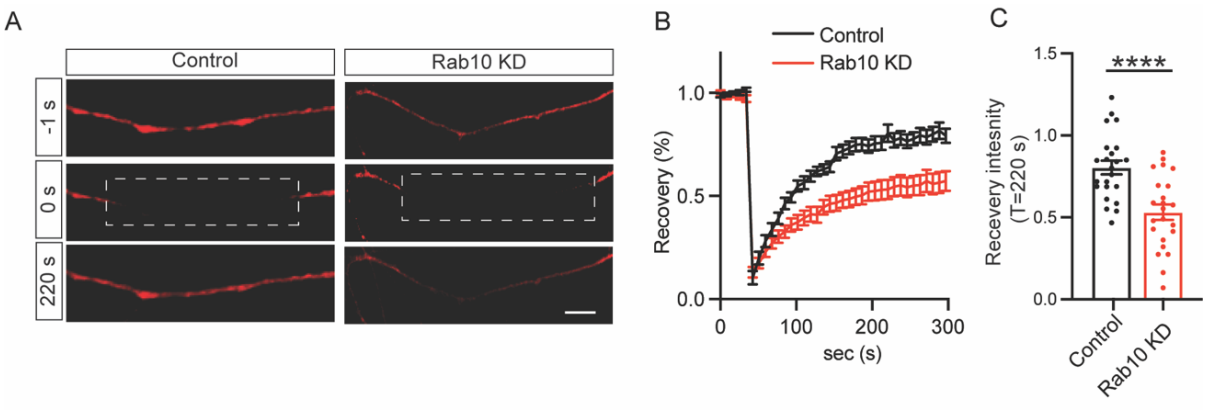

622
623 **Figure 4—figure supplement 2: Impaired ER dynamics in Rab10 KD neurons.**
624 (A) Representative time-lapse of ER-mCherry3 signal before (upper), upon (middle) and after
625 (bottom) photobleaching.
626 (B) Average normalized ER-mCherry3 fluorescence recovery after photobleaching in control and
627 Rab10 KD hippocampal neurons.
628 (C) Normalized ER-mCherry3 fluorescence recovery after photobleaching at T = 220 s in control
629 and Rab10 KD hippocampal neurons.
630 All Data are plotted as mean±s.e.m. (B, C) Control: N = 3, n = 23; Rab10 KD: N = 3, n = 23; (B, C) A
631 one-way ANOVA tested the significance of adding experimental group as a predictor. **** =
632 p<0.0001.

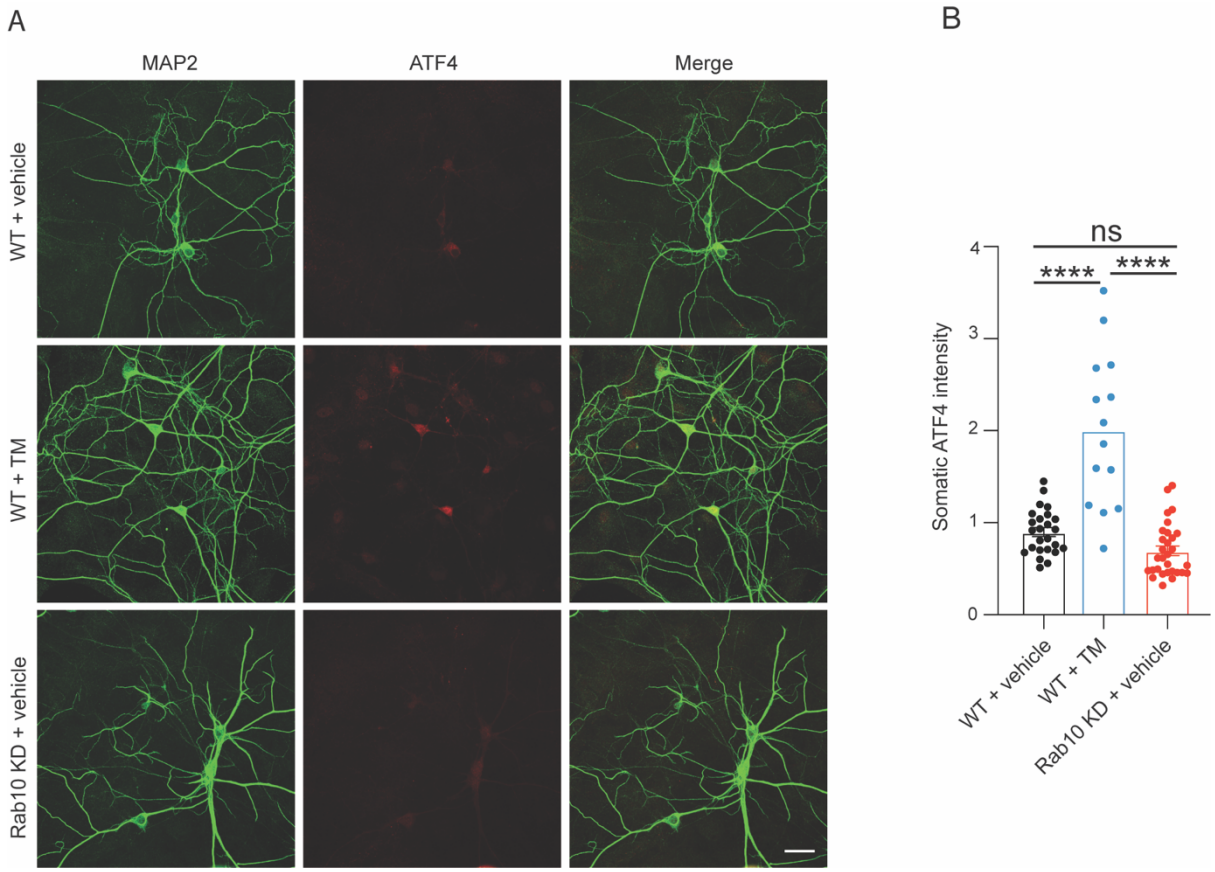

Figure 4—figure supplement 3: Rab10 depletion does not increase ER stress.

(A) Representative images of wild-type (WT) neurons treated with vehicle (top) or tunicamycin (TM, middle) and Rab10 KD neurons treated with vehicle (bottom). Neurons were stained for ATF4 and MAP2. Scale bar: 50 µm.

(B) Quantification of ATF4 intensity in soma from each condition. All data are presented as mean±s.e.m. WT + vehicle: N = 2, n = 25; WT + vehicle: N = 2, n = 30; Rab10 KD + vehicle: N = 2, n = 14. A one-way ANOVA tested the significance of adding experimental group as a predictor. **** = $p<0.0001$, ns = not significant.

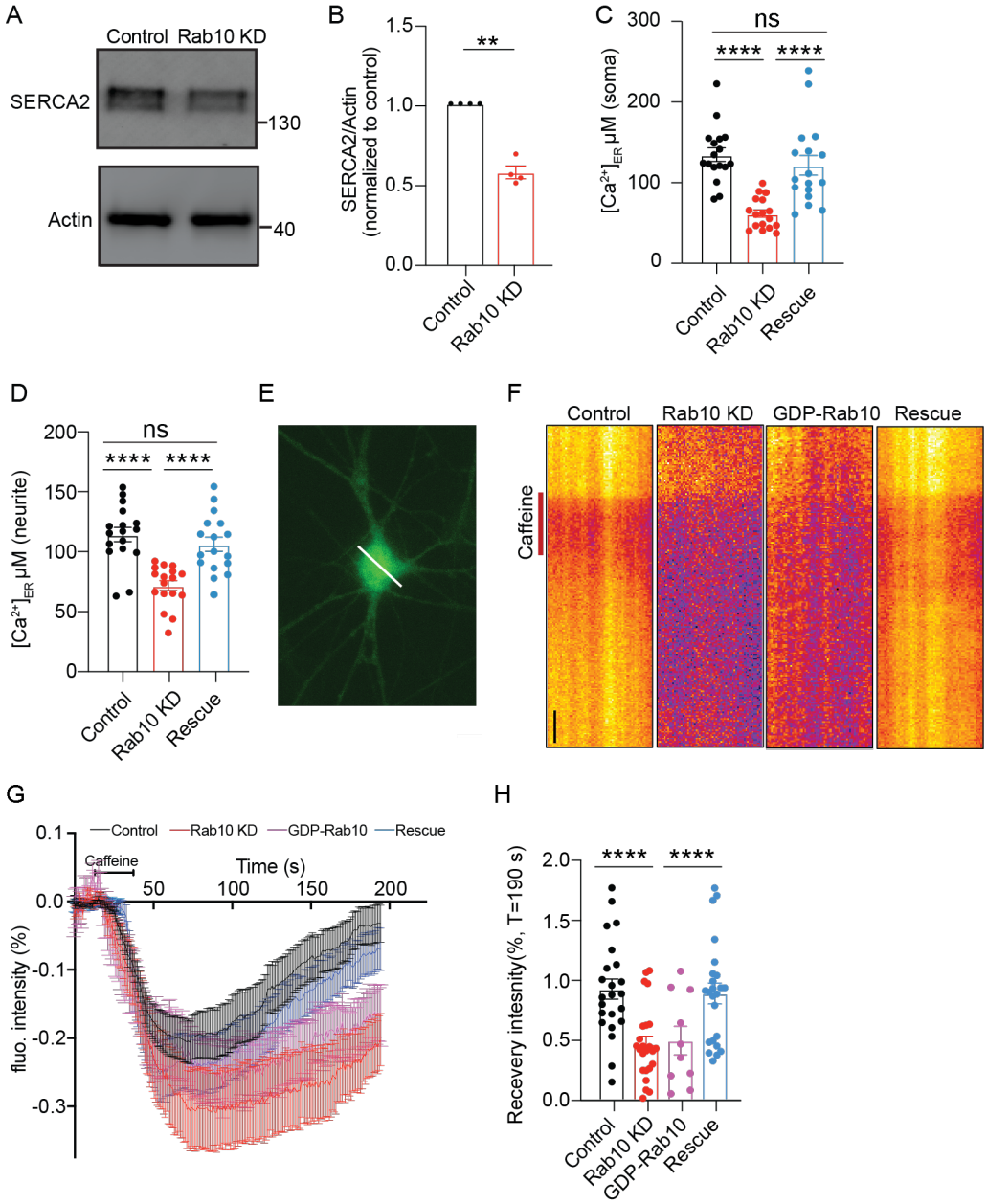

Figure 5: Reduced SERCA2 levels and impaired ER Ca^{2+} homeostasis in Rab10 KD neurons.

(A) Typical immunoblot showing reduced SERCA2 levels in Rab10 KD hippocampal neurons.

(B) Quantification of protein levels in Rab10 KD neurons normalized to control.

(C) Quantification of somatic ER Ca^{2+} concentration.

(D) Quantification of dendritic ER Ca^{2+} concentration.

649 (E) Representative image of a neuron infected with ER-GCaMP6-150 displayed with a pseudo
650 line. Scale bar: 3 µm.
651 (F) Typical kymographs of the somatic intensity of ER-GCaMP6-150 showing the intensity
652 decrease upon caffeine superfusion (red line), and the recovery in intensity after caffeine
653 washout. Scale bar: 10 s.
654 (G) Average normalized ER-GCaMP6-150 fluorescence recovery after caffeine treatment.
655 (H) Normalized ER-GCaMP6-150 fluorescence recovery after caffeine treatment at T = 190 s.
656 All Data are plotted as mean±s.e.m. (B) Control: N = 4, n = 4; Rab10 KD: N = 4, n = 4; (C-D)
657 Control: N = 3, n = 17; Rab10 KD: N = 3; n = 17; Rescue: N = 3, n = 17 (H) Control: N = 3, n = 23;
658 Rab10 KD: N = 3; n = 24; GDP-Rab10: n =3, n = 10; Rescue: N = 3, n = 24. A one-way ANOVA
659 tested the significance of adding experimental group as a predictor. **** = p<0.0001, *** = p<0.001,
660 ** = p<0.01, ns = not significant.
661

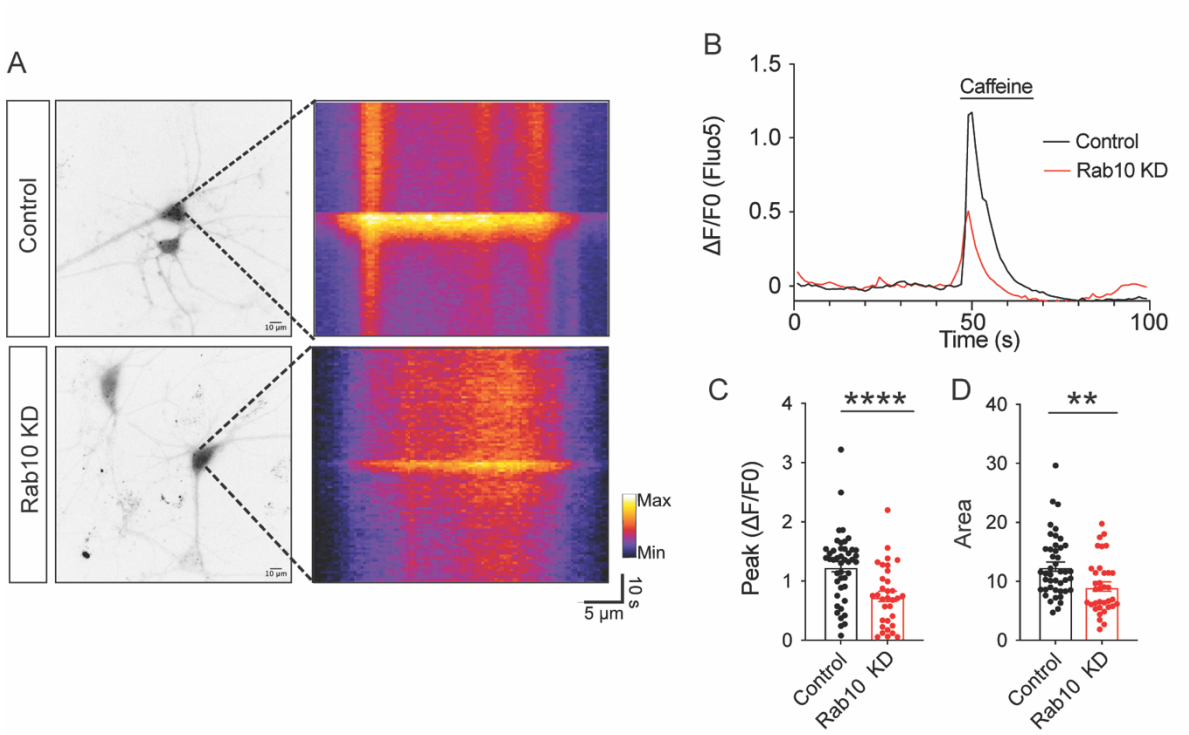

662
663 **Figure 5—figure supplement 1: Caffeine triggers less ER Ca^{2+} release in Rab10 KD neurons.**
664 (A) Left: representative cytosolic Fluo-5 AM signals upon Caffeine perfusion. Right:
665 representative kymographs of cytosolic Fluo-5 AM signals upon caffeine perfusion in somas.
666 (B) Average traces of Fluo-5 AM signals.
667 (C) Quantification of the peak values of the Fluo-5 AM fluorescence traces upon caffeine
668 perfusion.
669 (D) Quantification of the area under the curve (AUC) of the Fluo-5 AM fluorescence traces upon
670 caffeine perfusion.

671 All Data are plotted as mean±s.e.m. (C, D) Control: N = 3, n = 44; Rab10 KD: N = 3, n = 35; (C, D)
672 A one-way ANOVA tested the significance of adding experimental group as a predictor. **** =
673 p<0.0001, ** = p<0.01.
674

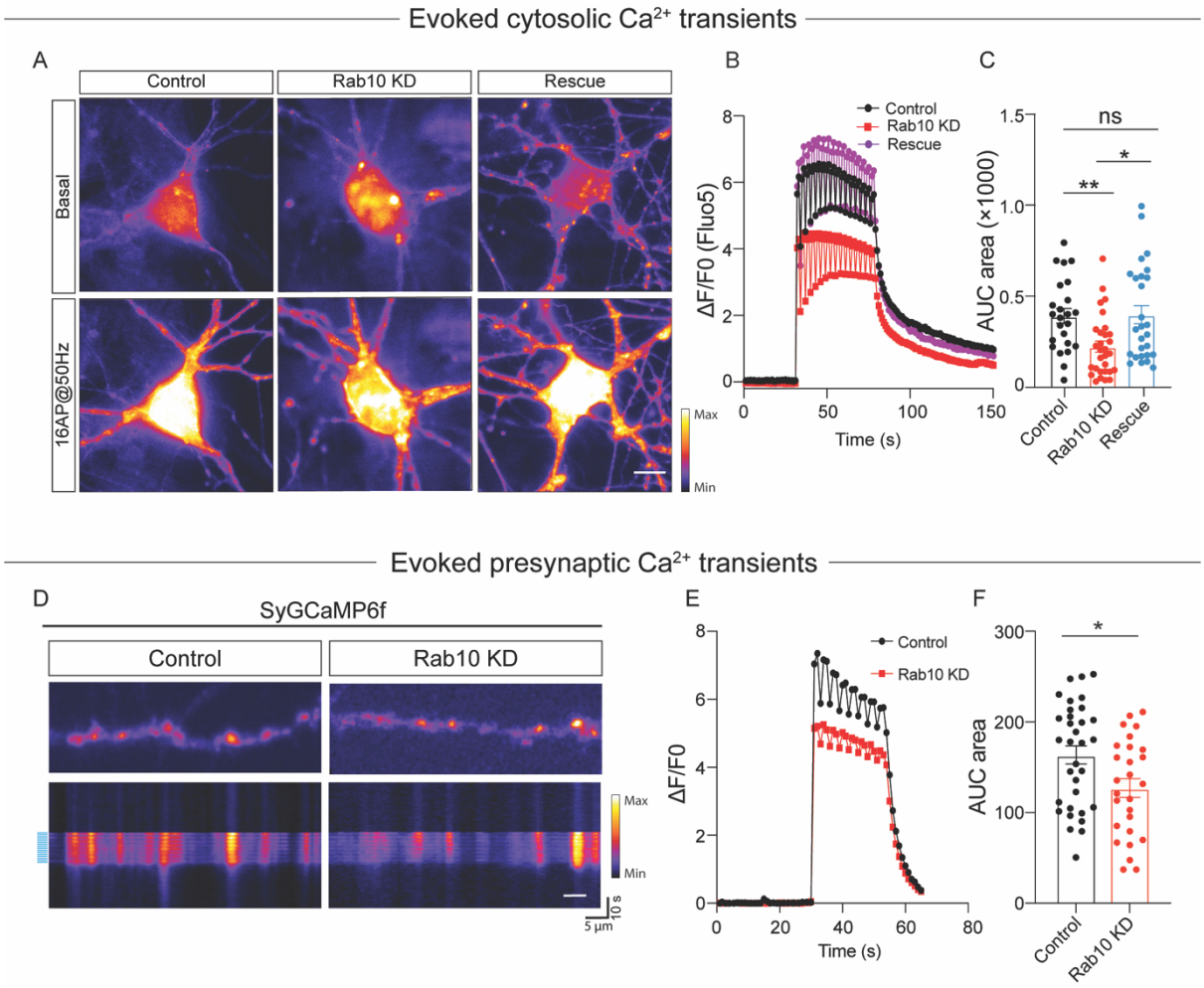

675

676 **Figure 6: Impaired neuronal Ca^{2+} influx triggered by electrical stimulation.**

677 (A) Representative time-lapse of cytosolic Fluo-5 AM upon electrical stimulation (16 APs, 50Hz)
678 in somas of hippocampal neurons. Scale bar: 10 µm.
679 (B) Average normalized response of somatic Fluo-5 AM fluorescence upon stimulation (16 APs,
680 50Hz) in hippocampal neurons.
681 (C) Quantification of the area under the curve (AUC) of the Fluo-5 AM fluorescence traces.
682 (D) Typical neurons infected with Synaptophysin-GCaMP6 (upper), typical kymograph of a
683 neurite (bottom) showing Synaptophysin-GCaMP6 intensity increase upon electrical
684 stimulation (16 APs, 50Hz, blue bars). Scale bar: 5µm.
685 (E) Average normalized response of Synaptophysin-GCaMP6 fluorescence intensity at
686 presynaptic boutons upon stimulation (16 APs, 50Hz) in hippocampal neurons.

687 (F) Quantification of the area under the curve (AUC) of the Synaptophysin-GCaMP6
688 fluorescence traces in control and Rab10 KD neurons.
689 All Data are plotted as mean±s.e.m. (C) Control: N = 4, n = 24; Rab10 KD: N = 4, n = 30; Rescue: N
690 = 4, n = 27. (F) Control: N = 3, n = 33; Rab10 KD: N = 3; n = 27. A one-way ANOVA tested the
691 significance of adding experimental group as a predictor. ** = p<0.01, * = p <0.05, ns = not
692 significant.
693

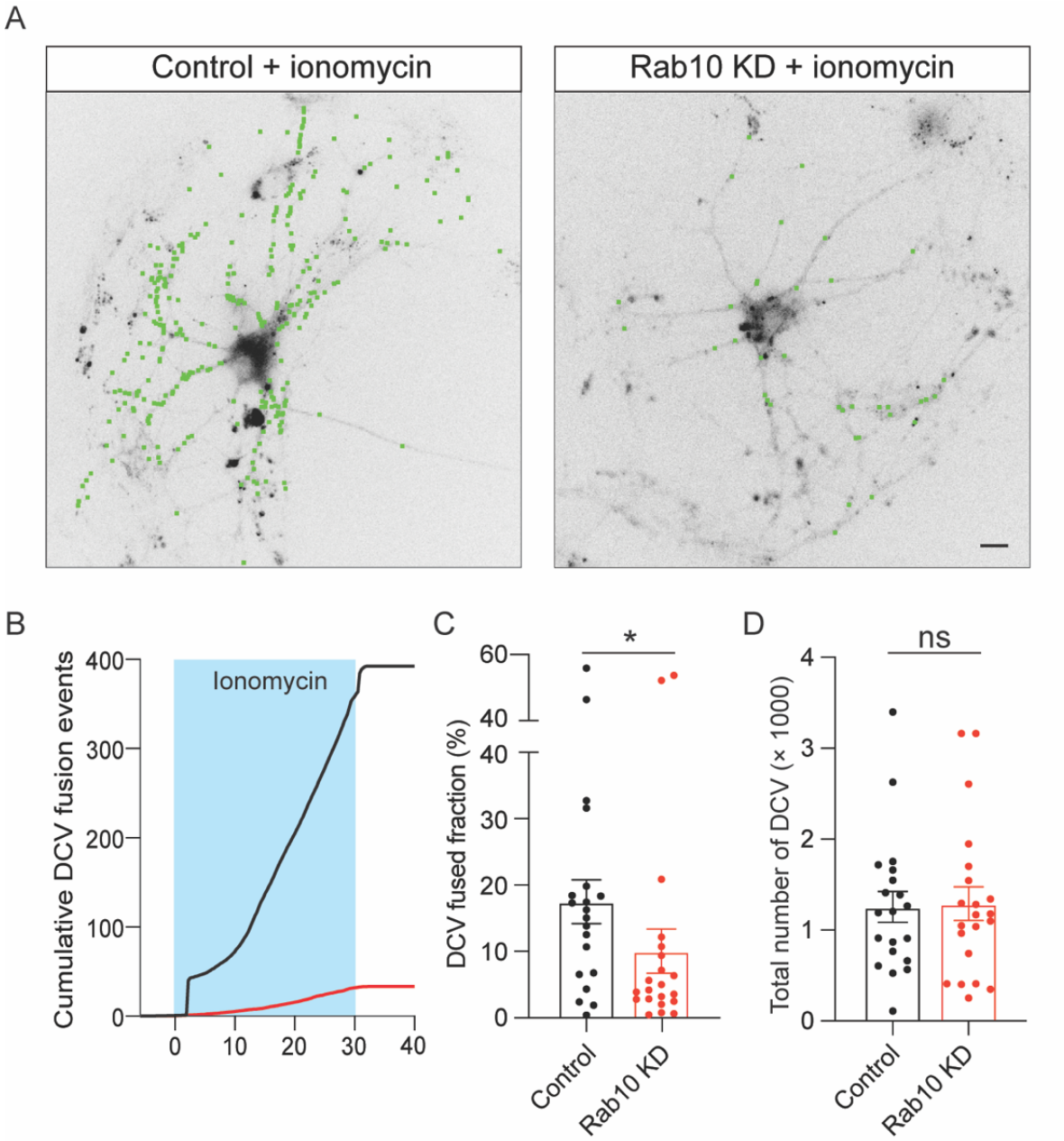

694
695 **Figure 7: Impaired DCV fusion induced by ionomycin in Rab10 KD neurons.**
696 (A) Representative neurons during electrical stimulation superimposed with NPY- pHluorin
697 fusion events (green dots). Scale bar: 10 µm.
698 (B) Cumulative plot of DCV fusion events per cell.

(C) Fraction of NPY-pHluorin-labeled DCVs fusing during stimulation.

(D) The total number of DCVs (total pool) of neurons analyzed in Figure 7B, measured as the number of NPY-pHluorin puncta upon NH_4Cl perfusion.

All Data are plotted as mean±s.e.m. (C, D) Control: N = 3, n = 20; Rab10 KD: N = 3, n = 21. (C, D) A one-way ANOVA tested the significance of adding experimental group as a predictor. * = p <0.05, ns = not significant.

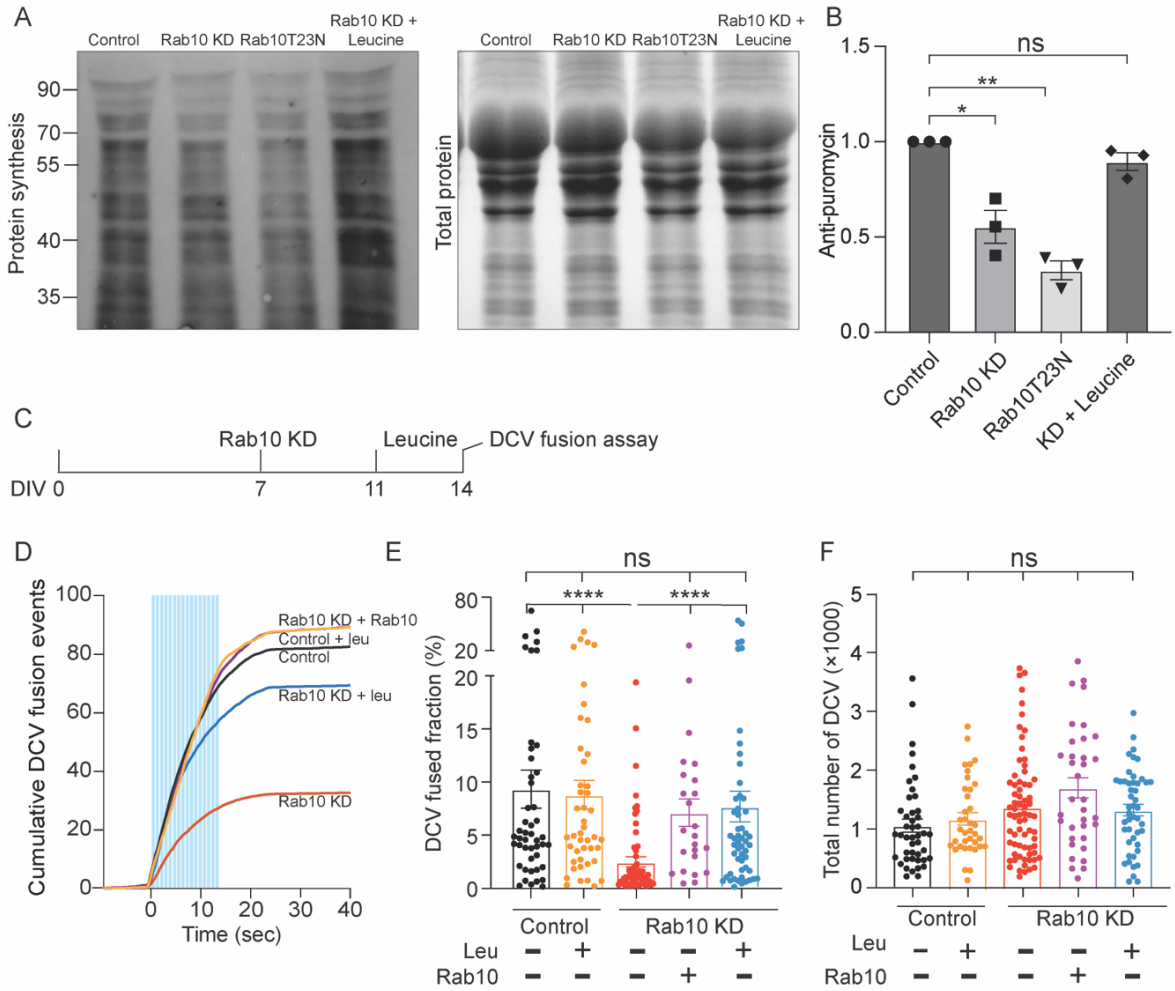

Figure 8: Leucine supplementation ameliorates the deficits in protein synthesis and neuropeptide release in Rab10 KD neurons.

(A) Representative western blot showing puromycinilated proteins as a measure for *de novo* protein synthesis in each condition.

(B) Quantification of puromycin intensity in each condition.

(C) Representation of the DCV fusion assay. Leucine (5 μM) was added to the culture media and incubated for 72 h before DCV fusion assay. DMSO (1‰) was used as a control.

(D) Cumulative plot of DCV fusion events per cell.

(E) Fraction of NPY-pHluorin-labeled DCVs fusing during stimulation.

716 (F) The total number of DCVs (total pool) of neurons analyzed in Figure 8D, E, measured as the
717 number of NPY-pHluorin puncta upon NH_4Cl perfusion.
718 All Data are plotted as mean±s.e.m. (B) All: N = 3, n = 3 (E, F) Control: N = 3, n = 47; Control + leu:
719 N = 3, n = 45; Rab10 KD: N = 3; n = 61; Rab10 + leu: N = 3, n = 54. Rab10 KD + Rab10: N = 3, n =
720 24. (B) One sample t-test. (E, F) A one-way ANOVA tested the significance of adding experimental
721 group as a predictor. ** = p<0.01, * = p <0.05, ns = not significant.
722

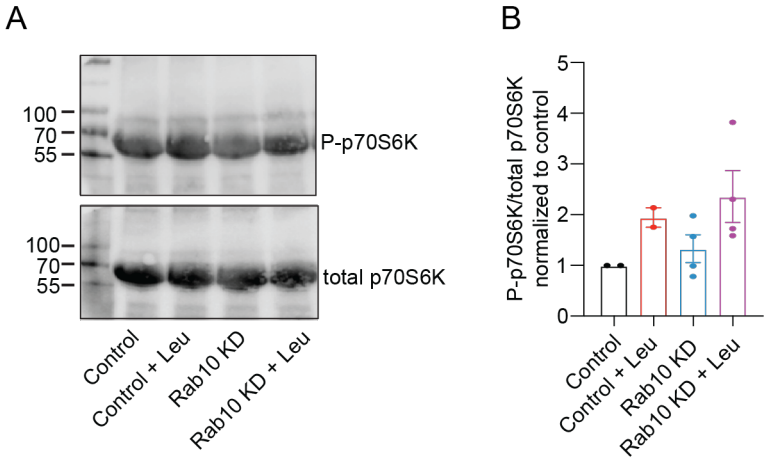

723
724
725 **Figure 8—figure supplement 1: Rab10 depletion does not upregulate mTORC1 pathway**
726 (A) Typical immunoblot showing pS6K1 levels in each condition.
727 (B) Quantification of relative pS6K1 levels in each condition. All Data are plotted as
728 mean±s.e.m. (B) Control, Control + Leu: N = 2, n = 2, Rab10 KD, Rab10 KD + Leu: N =
729 2, n = 4.

730

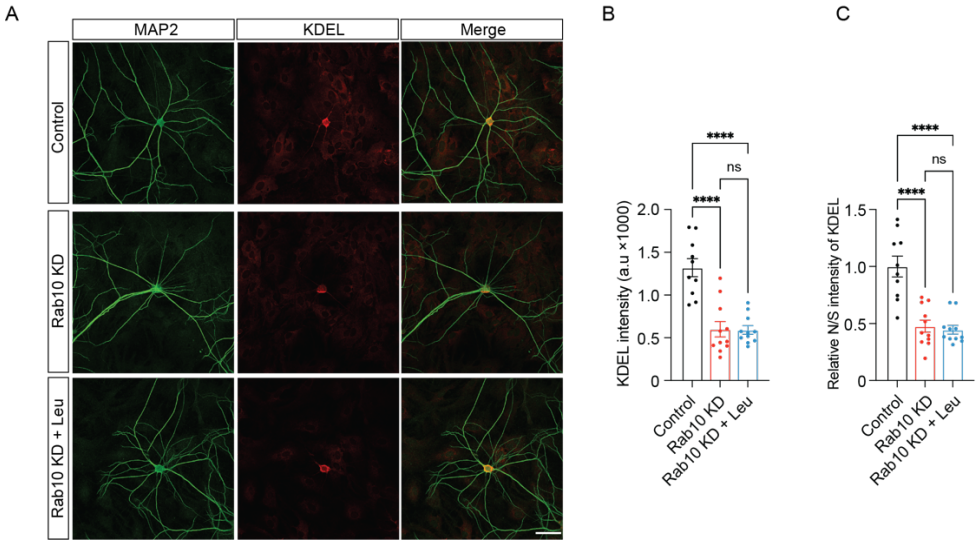

731

732 **Figure 8—figure supplement 2: Leucine supplementation does not rescue ER**
733 **morphological deficiency in Rab10 KD neurons**
734 (A) Typical examples showing the KDEL signals in each condition
735 (B) Quantification of RTN4 intensity in MAP2-positive dendrites.
736 (C) The ratio of neuritic to somatic RTN4 intensity (N/S).
737 All Data are plotted as mean±s.e.m. (B, C) Control: N = 3, n = 10; Rab10 KD: N = 3, n = 11; Rab10
738 KD + Leu: N = 3; n = 11. A one-way ANOVA tested the significance of adding experimental group
739 as a predictor. **** = p<0.0001, ns = not significant.

740

741

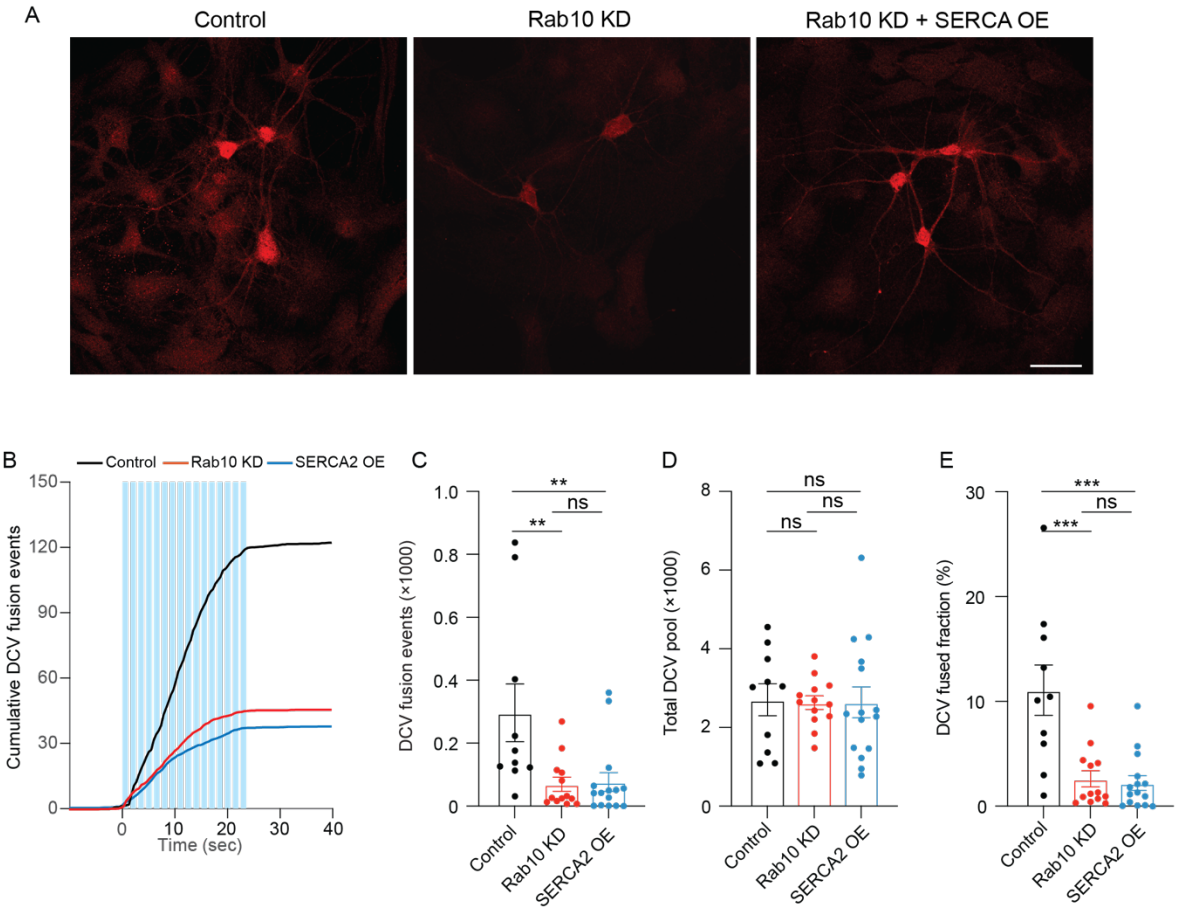

742

743 **Figure 8**—figure supplement 3: Overexpression of SERCA2 does not resuce the DCV fusion
744 deficits in Rab10 KD neurons.
745 (A)Typical examples showing the SERCA2 signals in each condition
746 (B) Cumulative plot of DCV fusion events per cell
747 (C) Summary graph of DCV fusion events per cell.
748 (D) Total number of DCVs (total pool) of neurons, measured as the number of NPY-pHluorin
749 puncta upon NH4Cl perfusion.

750 (E) Fraction of NPY-pHluorin-labeled DCV fusing during stimulation.
751 All Data are plotted as mean±s.e.m. (C-E) Control: N = 2, n = 10; Rab10 KD: N = 2, n = 13; SERCA2
752 OE: N = 2; n = 15. A one-way ANOVA tested the significance of adding experimental group as a
753 predictor. *** = p<0.001, ** = p<0.01, ns = not significant.

754
755
756
757

Materials and Methods

Key Resources Table

Reagent type (species) or resource	Designation	Source or reference	Identifiers	Additional information
gene (Mus musculus)	Rab10	NCBI	74173	
genetic reagent (Mus musculus)	C57BL/6 J	Charles River	Strain code 631	
genetic reagent (Rattus norvegicus)	Wistar (Crl:WI)	Charles River	Strain code 003	
antibody	MAP2 (chicken polyclonal)	Abcam	ab5392	1:200 (IF)
antibody	SMI312 (mouse polyclonal)	Eurogentec	SMI-312P-050	1:500 (IF)
antibody	synaptophysin 1 (guinea pig polyclonal)	Synaptic Systems	101004	1:500 (IF)
antibody	KDEL (mouse monoclonal)	Enzo Life Sciences	ADI-SPA-827-D	1:200 (IF)
antibody	RTN4 (rabbit polyclonal)	Novus Biologicals	NB100-56681	1:200 (IF)
antibody	SERCA2 (mouse monoclonal)	Santa Cruz	sc-376235	1:200 (IF)
antibody	Rab10	Protein Tech	11808-1-AP	1:2000 (WB)
antibody	Rab10	Abcam	Ab241060	1:2000 (WB)
antibody	Actin	Chemicon	MAB15	1:4000 (WB)
antibody	Puromycin	Bio Connect	MABE343	1:2500 (WB)

transfected construct (Mus musculus)	shRNA#9	This paper	-	Lentiviral construct to transfect and express the shRNA (see Materials and Methods)
transfected construct (Mus musculus)	shRNA#11	This paper	-	Lentiviral construct to transfect and express the shRNA (see Materials and Methods)
transfected construct (Mus musculus)	Control	This paper	-	Lentiviral construct to transfect and express the control (see Materials and Methods
recombinant DNA reagent	pLenti-Syn(pr)-NPY-pHluorin	PMID: 31679900	-	-
recombinant DNA reagent	pLenti-Syn(pr)-NPY-mCherry	PMID: 31679900	-	-
recombinant DNA reagent	pLenti-Syn(pr)-Synaptophysin-pHluorin	PMID: 34020952	-	-
recombinant DNA reagent	pLenti-Syn(pr)-Synaptophysin-GCaMP6	This paper	-	Generation of this reagent is described in Materials and Methods
recombinant DNA reagent	ER-GCaMP6-150	Addgene	#86918	-
recombinant DNA reagent	mCherry-ER3	Addgene	#55041	-
recombinant DNA reagent	EGFP-Rab10T23N	Addgene	#49545	-
peptide, recombinant protein	pLenti-Syn(pr)-Rab10-EGFP	This paper	-	Generation of this reagent is described in Materials and Methods

peptide, recombinant protein	2.5% trypsin	Gibco	15090046	-
peptide, recombinant protein	poly-L-ornithine	Worthington Biochemical Corporation	LS003127	-
peptide, recombinant protein	Laminin	Sigma Aldrich	L2020	-
peptide, recombinant protein	poly-D-lysine	Sigma Aldrich	P6407	-
peptide, recombinant protein	L-Leucine	Sigma Aldrich	L8000	-
peptide, recombinant protein	Tunicamycin	Sigma Aldrich	T7765-10MG	-
chemical compound, drug	Puromycin	Merck/Millipore	540222-25MG	-
chemical compound, drug	Ionomycin	Fisher Emergo	10429883	-
software, algorithm	TCE	Sigma Aldrich	115-20-8	-
software, algorithm	MATLAB	MathWorks	-	-
software, algorithm	Prism	GraphPad	-	-
other	Fiji/ImageJ	NIH	-	-

758 WB: western blot; IF: Immunofluorescence

759

760 **Laboratory animals and primary cultures**

761 All animals were bred and housed according to Institutional and Dutch governmental
762 guidelines and regulations. The primary neuronal culture was done as described before (Moro
763 et al., 2021; Persoon et al., 2019). Briefly, hippocampi or cortices were extracted from E18
764 wild type (WT) embryos in Hanks' balanced salt solution (Sigma Aldrich), supplemented
765 with 10mM HEPES (Gibco) and were digested with 0.25% trypsin (Gibco) for 20 min at
766 37°C. neurons were washed three times and dissociated with fire-polished Pasteur pipettes.
767 Dissociated neurons were spun down at 1000 rpm for 5 mins and resuspended in Neurobasal

768 medium (Gibco) supplemented with 2% B-27 (Gibco), 1.8% HEPES, 0.25% Glutamax
769 (Gibco) and 0.1% penicillin/streptomycin. For continental culture, hippocampal neurons were
770 plated at a density of 30,000 on pre-grown rat glia cells, generated by adding 25,000 glia cells
771 on 18 mm glass coverslips coated with 0.1 mg/ml poly-d-lysine (Sigma Aldrich) in 12-well
772 plates. For island culture, a density of 1,500 hippocampal neurons was plated on pre-grown
773 micro-glia islands, generated by plating 6,000 glia cells on 18 mm glass coverslips coated
774 with agarose and stamped with a solution of 0.1 mg/ml poly-d-lysine (Sigma Aldrich) and
775 0.7 mg/ml rat tail collagen (BD Biosciences). For western blot, cortical neurons were plated
776 at a density of 300,000 on 6-well plates coated with a solution of 0.0005% poly-l-ornithine
777 and laminin (2.5 µg/ml) (Sigma Aldrich). Neurons were kept in supplemented Neurobasal at
778 37°C and 5% CO2 for 14-16 days (DIV 14 -16).

779

780 **Plasmid and lentiviral infection**

781 NPY-pHluorin, NPY-mCherry, and Synaptophysin-pHluorin plasmids have been described
782 (Persoon et al., 2019). Synaptophysin-GCaMP6 was generated by adding GCaMP6 to the C
783 terminus of the mouse sequence of synaptophysin as previously reported as previously
784 reported (de Juan-Sanz et al., 2017). ER-GCaMP6-150, mCherry-ER3, and Rab10T23N were
785 purchased from Addgene (ER-GCaMP6-150: #86918; mCherry-ER3: #55041; Rab10T23N:
786 #49545). Rab10-EGFP construct was obtained from a mouse cDNA library by PCR and
787 labeled with EGFP at the C terminus. The target sequences of shRNA are as follows:
788 CGATGCCTTCAATACCACCTT (shRNA#9), GAGAGTTGTACCGAAAGGCAA
789 (shRNA#11), TTC TCCGAACGTGTCACGT (Control, scramble),
790 CGATGCATTTAACACAACCTT (Rab10 resistant to shRNA#9).
791 All plasmids were sequenced-verified and packed into lentiviral particles as described
792 previously (Naldini et al., 1996).

793 **Immunocytochemistry**

794 Neurons were fixed at DIV14-16 in freshly prepared 3.7% paraformaldehyde (EMS) for 20
795 min at room temperature and permeabilized with 0.5% Triton X-100 (Fisher Chemical) for 5
796 min, blocked with 0.1% TritonX-100 and 2% normal goat serum for 30 min. Incubation with
797 primary antibodies was done at room temperature for 2 h or overnight at 4 °C. After three
798 times of PBS washing, neurons were incubated with Alexa Fluor conjugated secondary

799 antibodies (1:1,000; Invitrogen) for 1 h at room temperature. Coverslips were mounted in
800 Mowiol (Sigma Aldrich) and imaged on a Zeiss LSM 510 confocal laser-scanning
801 microscope (40 × objective; NA 1.3) with LSM510 software (version 3.2 Zeiss) or on an A1R
802 Nikon confocal microscope with LU4A laser unit (40 × objective; NA 1.3) with NIS elements
803 software (version 4.60, Nikon). Images were acquired as Z-stack at a step of 0.5 µm. All
804 acquisition settings were kept constant for scans within each experiment. All solutions were
805 in phosphate-buffered saline (PBS; 137 mM NaCl, 2.7 mM KCl, 10 mM Na2HPO4, 1.8 mM
806 KH2PO4, pH 7.4). Primary antibodies used were: MAP2 (Abcam 1:200), SMI312
807 (Eurogentec, 1:500), synaptophysin 1 (SySy, 1:500), KDEL (Enzo life science, 1:200), RTN4
808 (NB100-56681, 1:200), ATF4 (CST, 1:200). To measure ATF4 intensity, neurons were
809 treated with 5 µg/ml tunicamycin (TM; Sigma Aldrich) or DMSO as vehicle for 24 h before
810 fixation. Analysis of staining intensity was done with ImageJ. Analysis of neuronal
811 morphology, synapses, or DCV number was performed using the custom-made software
812 SynD (Schmitz et al., 2011).

813

814 **Western blotting**

815 Cortical neurons were lysed at DIV 14. Lysates were run on a 10 % SDS-PAGE gel and
816 transferred to a polyvinylidene difluoride membrane (Bio-Rad). Membranes were blocked
817 with 5% milk (Merck) in PBS with 0.1% Tween 20 for 1 hour at room temperature and
818 incubated in primary antibodies overnight at 4 °C. Secondary alkaline phosphatase–
819 conjugated antibodies (1:10,000; Jackson ImmunoResearch) were incubated for 50 min at
820 room temperature. Membranes were visualized with AttoPhos (Promega) and scanned with
821 an FLA-5000 fluorescent image analyzer (Fujifilm). Band intensities of interests were
822 analyzed using Fiji and normalized to the intensity of a loading control (actin).

823 For *de novo*-synthesised proteins quantification, surface sensing of translation (SUnSET) was
824 performed as previously described (Schmidt et al., 2009). In brief, neurons were incubated
825 with 2µM puromycin (InvivoGen) for 30 min before harvesting lysates. Puromycinylated
826 proteins were detected with the anti-puromycin antibody by WB. To measure the total protein
827 level, 2,2,2-Trichloroethanol (TCE, Lot # BCBK5461V, Sigma Aldrich) was dissolved in the
828 gel buffer (0.5%) and gels were scanned with Gel Doc EZ Imager (BIO-RAD).

829 Antibodies used for WB: actin (1:4000; Chemicon), SERCA2 (Santa Cruz, 1:1000), Rab10
830 (Proteintech, 1:2000), Rab10 (Abcam, 1:2000), Puromycin (Bio Connect, 1:2500).

831

832

833 **Proteomics**

834 DIV14 cortical neurons were prepared as previously described (Gonzalez-Lozano et al.,
835 2019). In brief, neurons were washed three times with ice-cold PBS. Then, 500µl PBS
836 supplemented with a protease inhibitor cocktail (Roche) was added to each well and neurons
837 were collected by gentle scraping. Neurons were centrifuged for 5 mins at 3000 g at 4 °C and
838 the pellet was collected and lysed in Laemmli loading buffer (4%SDS, 100mM Tris pH 6.8,
839 200mM DTT, 20% glycerol, 0.04% bromophenol blue). In-gel digestion was performed
840 overnight at 37 °C with MS grade endo Trypsin/LysC (Promega). The digested peptides were
841 dried using a speedvac and stored at − 20 °C until further processed. An SDS-PAGE LC-
842 MS/MS approach was used for peptide identification as previously reported. SWATH data
843 were analyzed using Spectronaut 8.0 (49). The spectral library was created from the merging
844 of two data-dependent analyses of non-transfected hippocampal neuron culture and
845 hippocampal synaptosomes containing spike-in iRT peptides from Biognosys. The retention
846 time prediction was set to dynamic iRT; the cross-run normalization based on total peak areas
847 was enabled. Peptide abundances were exported and analyzed using R language for statistical
848 computation. Only peptides present in both control and transfected groups and quantified
849 with high confidence were included (i.e. q-value $\leq 10^{-3}$ over all samples in either group,
850 allowing for one outlier within each condition). Protein abundances were computed using
851 Spectronaut normalized peak area, and Loess normalized using the 'normalizeCyclicLoess'
852 function from the limma R package (fast method and 10 iterations) (50). Proteins with an
853 adjusted FDR ≤ 0.01 and Log2 fold change ≥ 0.56 were defined as significant hints. The
854 proteomics experiment presented in Fig 3 was conducted with two independent cultures with
855 four technical replicates for each condition. For the analysis, we only included peptides that
856 were consistently detected across all samples.

857

858 **Bioinformatics**

859 GO analysis on proteomics data was performed with Cytoscope plug-in ClueGO (Bindea et
860 al., 2009). The following settings were used for the biological process analysis in ClueGO:
861 Biological process (update: 25-05-2022), GO term grouping, GO tree interval was set 6-10,
862 GO term consists of min. 3 genes and min. 3% of the term. The GO fusion option was set as
863 true with a threshold of 50%. GO terms were grouped with a Kappa score threshold of 0.4
864 and named after the most significant GO term. Cellular component analysis: Cellular

865 component analysis (update: 25-05-2022), GO term grouping, GO tree interval was set 6-8,
866 GO term consists of min. 5 genes and min. 5% of the term. The GO fusion option was set as
867 true with a threshold of 50%. GO terms were grouped with a Kappa score threshold of 0.5
868 and named after the most significant GO term. All detected proteins were input as
869 background. Go analysis of synaptic proteins was done with SynGO as previously described
870 (Koopmans et al., 2019).
871

872 **Electron microscopy**

873 Hippocampal neurons plated on coated plates were infected with control or shRNA#9 at
874 DIV7 and fixed at DIV14 with 2.5% glutaraldehyde in 0.1 M cacodylate buffer (pH 7.4).
875 Samples were post-fixed for 1 h at room temperature in 1% osmium/1% ruthenium. After
876 dehydration by increasing ethanol concentrations (30%, 50%, 70%, 90%, 96% and 100%),
877 cells were embedded in EPON solution and polymerized for 72 h at 65°C. Glass coverslips
878 were removed by heating the sample with hot water. Regions with a high density of neurons
879 were selected under light microscopy and mounted on pre-polymerized EPON blocks.
880 Ultrathin sections (70-90 nm) were cut parallel to the cell monolayer and collected on single-
881 slot, formvar-coated copper grids, and stained in uranyl acetate and lead citrate (Leica EM
882 AC20). Sections were imaged in a JEOL1010 transmission electron microscope (JEOL) at 60
883 kV while being blinded for the experimental conditions. Synapses, somas, and DCV-rich
884 areas were photographed by a side-mounted Modera camera (EMSIS GmbH). For all
885 synaptic analyses, only synapses with intact synaptic plasma membranes with a recognizable
886 pre- and post-synaptic density and clear synaptic vesicle membranes were selected. DCV and
887 ER diameters were measured in iTEM software (Olympus) and synapse parameters were
888 quantified in a custom-written software running in MATLAB (MathWorks) while being
889 blinded for the experimental conditions.
890

891 **Live-cell imaging**

892 Neurons at DIV 14-16 were transferred to an imaging chamber and perfused with Tyrode's
893 solution (2 mM CaCl2, 2.5 mM KCl, 119 mM NaCl, 2 mM MgCl2, 30 mM glucose, 25 mM
894 HEPES; pH 7.4). Imaging was acquired on a custom build microscope (AxioObserver.Z1,
895 Zeiss) with 40 × oil objective (NA 1.3) and an EM-CCD camera (C9100-02; Hamamatsu,
896 pixel size 200 nm) unless otherwise specified. Electrode field stimulation was applied using a

897 stimulus generator (A-385, World Precision Instruments) controlled by a Master-8 (AMPI) to
898 deliver 1 ms pulses of 30 mA. Experiments were performed at room temperature.

899 For SypHy experiments, neurons were imaged for 30 s as a baseline and then stimulated with
900 electrical field stimulation for 5 s at 40 Hz. After 90 s, neurons were superfused with
901 modified Tyrode's solution containing NH_4Cl (2 mM CaCl2, 2.5 mM KCl, 119 mM NaCl, 2
902 mM MgCl2, 30 mM glucose, 25 mM Hepes, and 50 mM NH_4Cl (pH 7.4)) delivered by
903 gravity flow through a capillary placed above the neurons.
904 SV fusion analysis was performed as described previously (Moro et al., 2021). Briefly,
905 Regions of interest (ROIs) consisting of 6x6 pixels were placed on individual synapses
906 identified as increased signals after the NH_4Cl perfusion. Individual traces were analyzed
907 using a custom-made MATLAB (MathWorks) script. Synapses were quantified as active if
908 the maximum $\Delta F/F0$ value upon stimulation was $\geq 3 * StD(F0)$. Active synapses were pooled
909 per neuron. SV fusion fraction was calculated as the ΔFstimulation/ΔF NH_4Cl.
910 For DCV fusion experiments, the imaging included 30 s of baseline recording and then
911 stimulated with electrical field stimulation for 16 pulses of 50 AP at 50 Hz. Chemical
912 stimulation of 5 µM Ionomycin, (Fisher Emergo) dissolved in modified Tyrode's solution,
913 was applied through glass capillaries placed near the neuron by gravity flow. After 90s,
914 neurons were superfused with modified Tyrode's solution containing NH_4Cl. For the leucine
915 rescue experiment, neurons expressing NPY-pHluorin were treated with 5mM leucine three
916 days before live-cell imaging, or with dimethyl sulfoxide (DMSO) as a control.
917 DCV fusion events were analyzed as described previously (Persoon et al., 2019). Briefly,
918 DCV fusion events were detected by a rapid increase in fluorescence intensity. Regions of
919 interest (ROIs) consisting of 3x3 pixels were placed on the time-lapse recordings using a
920 custom-made script in Fiji. Resulting traces were evaluated using a custom-made script in
921 MATLAB, and only events with $F/F0 \geq 2$ SD and a rise time of less than 1 second were
922 recorded. F0 was calculated by averaging the first 10 frames of the time-lapse recording. The
923 total intracellular DCV pool was determined as the number of fluorescent puncta after the
924 superfusion of Tyrode's solution containing 50 mM NH_4Cl. The released fraction was
925 calculated by dividing the number of fusion events per neuron by the total intracellular pool
926 of DCVs.
927 For DCV transport experiments, neurons were imaged at DIV 14 in time-lapse recordings
928 (2Hz) at room temperature. Stacks were divided into 10x10 regions with the Grid function in
929 ImageJ, and transport was measured in five random regions (coordinates generated by

930 random number generation in MATLAB). Kymographs were generated in ImageJ
931 (MultipleKymograph, line width 3) and were analyzed with a deep learning-based software
932 (KymoButler) as previously described (Jakobs et al., 2019).
933

934 Ca^{2+} imaging

935 For cytosolic Ca^{2+} imaging, neurons were incubated with 1µM Fluo-5F-AM (Molecular
936 Probes, F14222; stock in DMSO) for 10 mins at 37 °C. For data shown in Figures 6D, E and
937 F neurons were perfused with normal Tyrode's solution and stimulated with the same pattern
938 used for DCV experiments.
939
940 For the caffeine-induced Ca^{2+} responses (Figure 5), neurons were perfused with Tyrode's
941 solution without Ca^{2+}. Fluorescent intensity in soma was measured with ImageJ. Normalized
942 ΔF/F0 data was calculated per neuron after background subtraction.
943
944 For synaptic Ca^{2+} imaging, neurons were infected with Synaptophysin-GCaMP6 at DIV 8
945 and imaged at DIV 14. Neurons were perfused with normal Tyrode's solution and stimulated
946 with the same pattern used for DCV experiments. 20 neurite-located ROIs (6x6 pixels) and a
947 background ROI were measured per cell. Normalized ΔF/F0 data was calculated per neuron
948 after background subtraction.
949
950 For ER Ca^{2+} measurement, neurons were infected with ER-GCAMP6-150 at DIV 8 and were
951 imaged at DIV 14 at room temperature. As previously described (de Juan-Sanz et al., 2017),
952 500 µM or 50 µM ionomycin was applied to saturate the ER-GCAMP6-150 signal in soma or
953 neurite respectively. $[Ca2+]_{ER}$ were calculated as follow:
954 $[Ca2+]_{ER}=Kd((Fr/Fmax-1/Rf)/(1-Fr/Fmax)^{1/}n$. Kd is the affinity constant of the indicator
955 (150 µM), Fr is the measured fluorescence at rest, Rf is the dynamic range (45) and n is the
956 Hill coefficient (1.6). Fmax values were not corrected for pH changes.
957
958 All Ca^{2+} imaging experiments were performed in an imaging buffer with an epifluorescence
959 microscope (Nikon Eclipse Ti) equipped with a 40X oil objective. Quantitative analysis and
960 image processing were performed using ImageJ.
961

962 Fluorescence recovery after photobleaching

963 Neurons were infected with mCherry-ER3 at DIV 9 and imaged at DIV 14 on a Nikon Ti-E
964 Eclipse inverted microscope controlled by NIS elements software. The acquisition was
965 performed with a 40X oil objective. After acquiring 10 pre-FRAP images (every 8.5 s), an
966 80-pixel long ROI on the proximal axon was photobleached with maximal laser power (10
967 iterations). Images were acquired for 300 s. The post-bleaching fluorescence intensity was
968 normalized to the baseline fluorescence (F0), which was defined as the average intensity of
969 10 frames before the onset of photobleaching.
970
971 Statistics
972 All Data are presented as mean ± SEM. Datasets on single neuron measurements consist of
973 several neuronal cultures (N = number of independent cultures). Within each culture,
974 different coverslips are infected with various viruses to create distinct experimental groups,
975 from which multiple observations (n = individual neurons) are taken. To account for the
976 nested nature of our datasets, a fixed linear regression was performed, in which culture was
977 included as a linear predictor. Possible outliers were identified using the ROUT method using
978 GraphPad Prism software and were excluded from the statistical analysis. A fixed linear
979 regression model was then fitted to the data using the lm() function in R. A one-way anova
980 (analysis of variance) was used to assess whether including the experimental group as a
981 second linear predictor (formula = y ~ Group + Culture) statistically improved the fit of a
982 model without group information (formula = y ~ 1 + Culture). Post-hoc analysis was
983 performed using emmeans() function with Turkey adjustment when more than two
984 experimental groups were present.
985

986 **Reference:**

987 Ailion, M., Hannemann, M., Dalton, S., Pappas, A., Watanabe, S., Hegermann, J., Liu, Q., Han,
988 H.-F., Gu, M., Goulding, M.Q., Sasidharan, N., Schuske, K., Hullett, P., Eimer, S.,
989 Jorgensen, E.M., 2014. Two Novel Rab2 Interactors Regulate Dense-core Vesicle
990 Maturation. Neuron 82, 167–180. https://doi.org/10.1016/j.neuron.2014.02.017
991 Ananieva, E., Powell, J., Hutson, S., 2016. Leucine Metabolism in T Cell Activation: mTOR
992 Signaling and Beyond. Adv. Nutr. Int. Rev. J. 7, 798S-805S.
993 https://doi.org/10.3945/an.115.011221

994 Arruda, A.P., Hotamisligil, G.S., 2015. Calcium Homeostasis and Organelle Function in the
995 Pathogenesis of Obesity and Diabetes. Cell Metab. 22, 381–397.
996 https://doi.org/10.1016/j.cmet.2015.06.010
997 Azouz, N.P., Zur, N., Efergan, A., Ohbayashi, N., Fukuda, M., Amihai, D., Hammel, I.,
998 Rothenberg, M.E., Sagi-Eisenberg, R., 2014. Rab5 Is a Novel Regulator of Mast Cell
999 Secretory Granules: Impact on Size, Cargo, and Exocytosis. J. Immunol. 192, 4043–
1000 4053. https://doi.org/10.4049/jimmunol.1302196
1001 Balkowiec, A., Katz, D.M., 2002. Cellular Mechanisms Regulating Activity-Dependent Release
1002 of Native Brain-Derived Neurotrophic Factor from Hippocampal Neurons. J.
1003 Neurosci. 22, 10399–10407. https://doi.org/10.1523/JNEUROSCI.22-23-10399.2002
1004 Barde, S., Aguila, J., Zhong, W., Solarz, A., Mei, I., Prud'homme, J., Palkovits, M., Turecki, G.,
1005 Mulder, J., Uhlén, M., Nagy, C., Mechawar, N., Hedlund, E., Hökfelt, T., 2022.
1006 Expression of substance P, NPY and their Receptors Is Altered in Major Depression.
1007 https://doi.org/10.1101/2022.12.14.516867
1008 Beck, B., 2000. Neuropeptides and obesity. Nutrition 16, 916–923.
1009 https://doi.org/10.1016/S0899-9007(00)00410-X
1010 Bindea, G., Mlecnik, B., Hackl, H., Charoentong, P., Tosolini, M., Kirilovsky, A., Fridman, W.-
1011 H., Pagès, F., Trajanoski, Z., Galon, J., 2009. ClueGO: a Cytoscape plug-in to decipher
1012 functionally grouped gene ontology and pathway annotation networks.
1013 Bioinformatics 25, 1091–1093. https://doi.org/10.1093/bioinformatics/btp101
1014 Britzolaki, A., Saurine, J., Flaherty, E., Thelen, C., Pitychoutis, P.M., 2018. The SERCA2: A
1015 Gatekeeper of Neuronal Calcium Homeostasis in the Brain. Cell. Mol. Neurobiol. 38,
1016 981–994. https://doi.org/10.1007/s10571-018-0583-8
1017 Cajigas, I.J., Will, T., Schuman, E.M., 2010. Protein homeostasis and synaptic plasticity.
1018 EMBO J. 29, 2746–2752. https://doi.org/10.1038/emboj.2010.173
1019 Cawley, N.X., Li, Z., Loh, Y.P., 2016. 60 YEARS OF POMC: Biosynthesis, trafficking, and
1020 secretion of pro-opiomelanocortin-derived peptides. J. Mol. Endocrinol. 56, T77-97.
1021 https://doi.org/10.1530/JME-15-0323
1022 Chen, C.C.-H., Schweinsberg, P.J., Vashist, S., Mareiniss, D.P., Lambie, E.J., Grant, B.D., 2006.
1023 RAB-10 Is Required for Endocytic Recycling in the Caenorhabditis elegans Intestine.
1024 Mol. Biol. Cell 17, 1286–1297. https://doi.org/10.1091/mbc.E05-08-0787

1025 Cm, P., A, M., Jp, N., M, F., Jh, B., S, A., N, D., Jr, van W., Rf, T., M, V., 2018. Pool size
1026 estimations for dense-core vesicles in mammalian CNS neurons [WWW Document].
1027 EMBO J. https://doi.org/10.15252/embj.201899672
1028 de Juan-Sanz, J., Holt, G.T., Schreiter, E.R., de Juan, F., Kim, D.S., Ryan, T.A., 2017. Axonal
1029 endoplasmic reticulum Ca2+ content controls release probability in CNS nerve
1030 terminals. Neuron 93, 867-881.e6. https://doi.org/10.1016/j.neuron.2017.01.010
1031 Deng, C., Moradi, M., Reinhard, S., Ji, C., Jablonka, S., Hennlein, L., Lüningschrör, P., Doose,
1032 S., Sauer, M., Sendtner, M., 2021. Dynamic remodeling of ribosomes and
1033 endoplasmic reticulum in axon terminals of motoneurons. J. Cell Sci. 134, jcs258785.
1034 https://doi.org/10.1242/jcs.258785
1035 Droz, B., Rambourg, A., Koenig, H.L., 1975. The smooth endoplasmic reticulum: structure
1036 and role in the renewal of axonal membrane and synaptic vesicles by fast axonal
1037 tranport. Brain Res. 93, 1–13. https://doi.org/10.1016/0006-8993(75)90282-6
1038 Edwards, S.L., Charlie, N.K., Richmond, J.E., Hegermann, J., Eimer, S., Miller, K.G., 2009.
1039 Impaired dense core vesicle maturation in Caenorhabditis elegans mutants lacking
1040 Rab2. J. Cell Biol. 186, 881–895. https://doi.org/10.1083/jcb.200902095
1041 Emperador-Melero, J., Huson, V., van Weering, J., Bollmann, C., Fischer von Mollard, G.,
1042 Toonen, R.F., Verhage, M., 2018. Vti1a/b regulate synaptic vesicle and dense core
1043 vesicle secretion via protein sorting at the Golgi. Nat. Commun. 9, 3421.
1044 https://doi.org/10.1038/s41467-018-05699-z
1045 Endo, M., 1975. Mechanism of Action of Caffeine on the Sarcoplasmic Reticulum of Skeletal
1046 Muscle. Proc. Jpn. Acad. 51, 479–484. https://doi.org/10.2183/pjab1945.51.479
1047 English, A.R., Voeltz, G.K., 2013. Rab10 GTPase regulates ER dynamics and morphology. Nat.
1048 Cell Biol. 15, 169–178. https://doi.org/10.1038/ncb2647
1049 Farina, M., van de Bospoort, R., He, E., Persoon, C.M., van Weering, J.R., Broeke, J.H.,
1050 Verhage, M., Toonen, R.F., 2015. CAPS-1 promotes fusion competence of stationary
1051 dense-core vesicles in presynaptic terminals of mammalian neurons. eLife 4, e05438.
1052 https://doi.org/10.7554/eLife.05438
1053 Fu, S., Yang, L., Li, P., Hofmann, O., Dicker, L., Hide, W., Lin, X., Watkins, S.M., Ivanov, A.R.,
1054 Hotamisligil, G.S., 2011. Aberrant lipid metabolism disrupts calcium homeostasis
1055 causing liver endoplasmic reticulum stress in obesity. Nature 473, 528–531.
1056 https://doi.org/10.1038/nature09968

1057 Fujimoto, S., Yamamoto, K., Kuba, K., Morita, K., Kato, E., 1980. Calcium localization in the
1058 sympathetic ganglion of the bullfrog and effects of caffeine. Brain Res. 202, 21–32.
1059 Gärtner, A., Staiger, V., 2002. Neurotrophin secretion from hippocampal neurons evoked by
1060 long-term-potentiation-inducing electrical stimulation patterns. Proc. Natl. Acad. Sci.
1061 99, 6386–6391. https://doi.org/10.1073/pnas.092129699
1062 Granseth, B., Odermatt, B., Royle, S.J., Lagnado, L., 2006. Clathrin-Mediated Endocytosis Is
1063 the Dominant Mechanism of Vesicle Retrieval at Hippocampal Synapses. Neuron 51,
1064 773–786. https://doi.org/10.1016/j.neuron.2006.08.029
1065 Hannemann, M., Sasidharan, N., Hegermann, J., Kutscher, L.M., Koenig, S., Eimer, S., 2012.
1066 TBC-8, a Putative RAB-2 GAP, Regulates Dense Core Vesicle Maturation in
1067 Caenorhabditis elegans. PLOS Genet. 8, e1002722.
1068 https://doi.org/10.1371/journal.pgen.1002722
1069 Hartmann, M., Heumann, R., Lessmann, V., 2001. Synaptic secretion of BDNF after high-
1070 frequency stimulation of glutamatergic synapses. EMBO J. 20, 5887–5897.
1071 https://doi.org/10.1093/emboj/20.21.5887
1072 Heidelberger, R., Heinemann, C., Neher, E., Matthews, G., 1994. Calcium dependence of the
1073 rate of exocytosis in a synaptic terminal. Nature 371, 513–515.
1074 https://doi.org/10.1038/371513a0
1075 Holt, C.E., Martin, K.C., Schuman, E.M., 2019. Local translation in neurons: visualization and
1076 function. Nat. Struct. Mol. Biol. 26, 557–566. https://doi.org/10.1038/s41594-019-
1077 0263-5
1078 Homma, Y., Hiragi, S., Fukuda, M., 2020. Rab family of small GTPases: an updated view on
1079 their regulation and functions. FEBS J. https://doi.org/10.1111/febs.15453
1080 Karagas, N.E., Venkatachalam, K., 2019. Roles for the Endoplasmic Reticulum in Regulation
1081 of Neuronal Calcium Homeostasis. Cells 8, 1232.
1082 https://doi.org/10.3390/cells8101232
1083 Kiral, F.R., Kohrs, F.E., Jin, E.J., Hiesinger, P.R., 2018. Rab GTPases and Membrane Trafficking
1084 in Neurodegeneration. Current Biology 28, R471–R486.
1085 https://doi.org/10.1016/j.cub.2018.02.010
1086 Koga, H., Kaushik, S., Cuervo, A.M., 2011. Protein homeostasis and aging: The importance of
1087 exquisite quality control. Ageing Res. Rev., The Longevity Consortium 10, 205–215.
1088 https://doi.org/10.1016/j.arr.2010.02.001

1089 Koopmans, F., van Nierop, P., Andres-Alonso, M., Byrnes, A., Cijsouw, T., Coba, M.P.,
1090 Cornelisse, L.N., Farrell, R.J., Goldschmidt, H.L., Howrigan, D.P., Hussain, N.K., Imig,
1091 C., de Jong, A.P.H., Jung, H., Kohansalnodehi, M., Kramarz, B., Lipstein, N., Lovering,
1092 R.C., MacGillavry, H., Mariano, V., Mi, H., Ninov, M., Osumi-Sutherland, D., Pielot, R.,
1093 Smalla, K.-H., Tang, H., Tashman, K., Toonen, R.F.G., Verpelli, C., Reig-Viader, R.,
1094 Watanabe, K., van Weering, J., Achsel, T., Ashrafi, G., Asi, N., Brown, T.C., De Camilli,
1095 P., Feuermann, M., Foulger, R.E., Gaudet, P., Joglekar, A., Kanellopoulos, A.,
1096 Malenka, R., Nicoll, R.A., Pulido, C., de Juan-Sanz, J., Sheng, M., Südhof, T.C., Tilgner,
1097 H.U., Bagni, C., Bayés, À., Biederer, T., Brose, N., Chua, J.J.E., Dieterich, D.C.,
1098 Gundelfinger, E.D., Hoogenraad, C., Huganir, R.L., Jahn, R., Kaeser, P.S., Kim, E.,
1099 Kreutz, M.R., McPherson, P.S., Neale, B.M., O'Connor, V., Posthuma, D., Ryan, T.A.,
1100 Sala, C., Feng, G., Hyman, S.E., Thomas, P.D., Smit, A.B., Verhage, M., 2019. SynGO:
1101 An Evidence-Based, Expert-Curated Knowledge Base for the Synapse. Neuron 103,
1102 217-234.e4. https://doi.org/10.1016/j.neuron.2019.05.002
1103 Laguesse, S., Ron, D., 2020. Protein Translation and Psychiatric Disorders. The Neuroscientist
1104 26, 21–42. https://doi.org/10.1177/1073858419853236
1105 Larance, M., Ramm, G., Stöckli, J., Dam, E.M. van, Winata, S., Wasinger, V., Simpson, F.,
1106 Graham, M., Junutula, J.R., Guilhaus, M., James, D.E., 2005. Characterization of the
1107 Role of the Rab GTPase-activating Protein AS160 in Insulin-regulated GLUT4
1108 Trafficking *. J. Biol. Chem. 280, 37803–37813.
1109 https://doi.org/10.1074/jbc.M503897200
1110 Laurent, P., Ch'ng, Q., Jospin, M., Chen, C., Lorenzo, R., de Bono, M., 2018. Genetic
1111 dissection of neuropeptide cell biology at high and low activity in a defined sensory
1112 neuron. Proc. Natl. Acad. Sci. 115, E6890–E6899.
1113 https://doi.org/10.1073/pnas.1714610115
1114 Lazo, O.M., Schiavo, G., 2023. Rab10 regulates the sorting of internalised TrkB for
1115 retrograde axonal transport. eLife 12, e81532. https://doi.org/10.7554/eLife.81532
1116 Lund, V.K., Lycas, M.D., Schack, A., Andersen, R.C., Gether, Ui., Kjaerulff, O., 2020. Rab2
1117 drives axonal transport of dense core vesicles and lysosomal organelles (preprint).
1118 Neuroscience. https://doi.org/10.1101/2020.06.03.131672

1119 Lv, P., Sheng, Y., Zhao, Z., Zhao, W., Gu, L., Xu, T., Song, E., 2015. Targeted disruption of
1120 Rab10 causes early embryonic lethality. Protein Cell 6, 463–467.
1121 https://doi.org/10.1007/s13238-015-0150-8
1122 Malva, J.O., Xapelli, S., Baptista, S., Valero, J., Agasse, F., Ferreira, R., Silva, A.P., 2012.
1123 Multifaces of neuropeptide Y in the brain--neuroprotection, neurogenesis and
1124 neuroinflammation. Neuropeptides 46, 299–308.
1125 https://doi.org/10.1016/j.npep.2012.09.001
1126 Mîinea, C.P., Sano, H., Kane, S., Sano, E., Fukuda, M., Peränen, J., Lane, W.S., Lienhard, G.E.,
1127 2005. AS160, the Akt substrate regulating GLUT4 translocation, has a functional Rab
1128 GTPase-activating protein domain. Biochem. J. 391, 87–93.
1129 https://doi.org/10.1042/BJ20050887
1130 Moro, A., Nifterick, A. van, Toonen, R.F., Verhage, M., 2021. Dynamin controls neuropeptide
1131 secretion by organizing dense-core vesicle fusion sites. Sci. Adv. 7, eabf0659.
1132 https://doi.org/10.1126/sciadv.abf0659
1133 Moro, A., Woerden, G.M. van, Toonen, R.F., Verhage, M., 2020. CaMKII controls
1134 neuromodulation via neuropeptide gene expression and axonal targeting of
1135 neuropeptide vesicles. PLOS Biol. 18, e3000826.
1136 https://doi.org/10.1371/journal.pbio.3000826
1137 Moya-Alvarado, G., Tiburcio-Felix, R., Ibáñez, M.R., Aguirre-Soto, A.A., Guerra, M.V., Wu, C.,
1138 Mobley, W.C., Perlson, E., Bronfman, F.C., 2023. BDNF/TrkB signaling endosomes in
1139 axons coordinate CREB/mTOR activation and protein synthesis in the cell body to
1140 induce dendritic growth in cortical neurons. eLife 12, e77455.
1141 https://doi.org/10.7554/eLife.77455
1142 Nassal, J.P., Murphy, F.H., Toonen, R.F., Verhage, M., 2022. Differential axonal trafficking of
1143 Neuropeptide Y-, LAMP1-, and RAB7-tagged organelles in vivo. eLife 11, e81721.
1144 https://doi.org/10.7554/eLife.81721
1145 Patel, J.C., Witkovsky, P., Avshalumov, M.V., Rice, M.E., 2009. Mobilization of Calcium from
1146 Intracellular Stores Facilitates Somatodendritic Dopamine Release. J. Neurosci. 29,
1147 6568–6579. https://doi.org/10.1523/JNEUROSCI.0181-09.2009
1148 Periasamy, M., Kalyanasundaram, A., 2007. SERCA pump isoforms: Their role in calcium
1149 transport and disease. Muscle Nerve 35, 430–442.
1150 https://doi.org/10.1002/mus.20745

1151 Persoon, C.M., Hoogstraaten, R.I., Nassal, J.P., van Weering, J.R.T., Kaeser, P.S., Toonen, R.F.,
1152 Verhage, M., 2019. The RAB3-RIM Pathway Is Essential for the Release of
1153 Neuropeptides. Neuron 104, 1065-1080.e12.
1154 https://doi.org/10.1016/j.neuron.2019.09.015
1155 Poo, M.M., 2001. Neurotrophins as synaptic modulators. Nat. Rev. Neurosci. 2, 24–32.
1156 https://doi.org/10.1038/35049004
1157 Sah, R., Geracioti, T.D., 2013. Neuropeptide Y and posttraumatic stress disorder. Mol.
1158 Psychiatry 18, 646–655. https://doi.org/10.1038/mp.2012.101
1159 Salio, C., Lossi, L., Ferrini, F., Merighi, A., 2006. Neuropeptides as synaptic transmitters. Cell
1160 Tissue Res. 326, 583–598. https://doi.org/10.1007/s00441-006-0268-3
1161 Sano, H., Eguez, L., Teruel, M.N., Fukuda, M., Chuang, T.D., Chavez, J.A., Lienhard, G.E.,
1162 McGraw, T.E., 2007. Rab10, a Target of the AS160 Rab GAP, Is Required for Insulin-
1163 Stimulated Translocation of GLUT4 to the Adipocyte Plasma Membrane. Cell Metab.
1164 5, 293–303. https://doi.org/10.1016/j.cmet.2007.03.001
1165 Sasidharan, N., Sumakovic, M., Hannemann, M., Hegermann, J., Liewald, J.F., Olendrowitz,
1166 C., Koenig, S., Grant, B.D., Rizzoli, S.O., Gottschalk, A., Eimer, S., 2012. RAB-5 and
1167 RAB-10 cooperate to regulate neuropeptide release in Caenorhabditis elegans. Proc.
1168 Natl. Acad. Sci. U. S. A. 109, 18944–18949.
1169 https://doi.org/10.1073/pnas.1203306109
1170 Schmidt, E.K., Clavarino, G., Ceppi, M., Pierre, P., 2009. SUnSET, a nonradioactive method to
1171 monitor protein synthesis. Nat. 6, 275–277. https://doi.org/10.1038/nmeth.1314
1172 Shakiryanova, D., Klose, M.K., Zhou, Y., Gu, T., Deitcher, D.L., Atwood, H.L., Hewes, R.S.,
1173 Levitan, E.S., 2007. Presynaptic Ryanodine Receptor-Activated Calmodulin Kinase II
1174 Increases Vesicle Mobility and Potentiates Neuropeptide Release. J. Neurosci. 27,
1175 7799–7806. https://doi.org/10.1523/JNEUROSCI.1879-07.2007
1176 Shih, Y.-T., Hsueh, Y.-P., 2016. VCP and ATL1 regulate endoplasmic reticulum and protein
1177 synthesis for dendritic spine formation. Nat. Commun. 7, 11020.
1178 https://doi.org/10.1038/ncomms11020
1179 Sinha, R., Ahmed, S., Jahn, R., Klingauf, J., 2011. Two synaptobrevin molecules are sufficient
1180 for vesicle fusion in central nervous system synapses. Proc. Natl. Acad. Sci. U. S. A.
1181 108, 14318–14323. https://doi.org/10.1073/pnas.1101818108

1182 Sumakovic, M., Hegermann, J., Luo, L., Husson, S.J., Schwarze, K., Olendrowitz, C., Schoofs,
1183 L., Richmond, J., Eimer, S., 2009. UNC-108/RAB-2 and its effector RIC-19 are involved
1184 in dense core vesicle maturation in Caenorhabditis elegans. J. Cell Biol. 186, 897–
1185 914. https://doi.org/10.1083/jcb.200902096
1186 Takamori, S., Holt, M., Stenius, K., Lemke, E.A., Grønborg, M., Riedel, D., Urlaub, H., Schenck,
1187 S., Brügger, B., Ringler, P., Müller, S.A., Rammner, B., Gräter, F., Hub, J.S., Groot,
1188 B.L.D., Mieskes, G., Moriyama, Y., Klingauf, J., Grubmüller, H., Heuser, J., Wieland, F.,
1189 Jahn, R., 2006. Molecular Anatomy of a Trafficking Organelle. Cell 127, 831–846.
1190 https://doi.org/10.1016/j.cell.2006.10.030
1191 Taoufiq, Z., Ninov, M., Villar-Briones, A., Wang, H.-Y., Sasaki, T., Roy, M.C., Beauchain, F.,
1192 Mori, Y., Yoshida, T., Takamori, S., Jahn, R., Takahashi, T., 2020. Hidden proteome of
1193 synaptic vesicles in the mammalian brain. Proc. Natl. Acad. Sci. 117, 33586–33596.
1194 https://doi.org/10.1073/pnas.2011870117
1195 Taylor, C.A., Yan, J., Howell, A.S., Dong, X., Shen, K., 2015. RAB-10 Regulates Dendritic
1196 Branching by Balancing Dendritic Transport. PLOS Genet. 11, e1005695.
1197 https://doi.org/10.1371/journal.pgen.1005695
1198 Thomas, P., Wong, J.G., Lee, A.K., Almers, W., 1993. A low affinity Ca2+ receptor controls
1199 the final steps in peptide secretion from pituitary melanotrophs. Neuron 11, 93–104.
1200 https://doi.org/10.1016/0896-6273(93)90274-U
1201 Tooze, S.A., Martens, G.J.M., Huttner, W.B., 2001. Secretory granule biogenesis: rafting to
1202 the SNARE. Trends Cell Biol. 11, 116–122. https://doi.org/10.1016/S0962-
1203 8924(00)01907-3
1204 Valadas, J.S., Esposito, G., Vandekerkhove, D., Miskiewicz, K., Deaulmerie, L., Raitano, S.,
1205 Seibler, P., Klein, C., Verstreken, P., 2018. ER Lipid Defects in Neuropeptidergic
1206 Neurons Impair Sleep Patterns in Parkinson's Disease. Neuron 98, 1155-1169.e6.
1207 https://doi.org/10.1016/j.neuron.2018.05.022
1208 van de Bospoort, R., Farina, M., Schmitz, S.K., de Jong, A., de Wit, H., Verhage, M., Toonen,
1209 R.F., 2012. Munc13 controls the location and efficiency of dense-core vesicle release
1210 in neurons. J. Cell Biol. 199, 883–891. https://doi.org/10.1083/jcb.201208024
1211 Verhage, M., McMahon, H.T., Ghijsen, W.E.J.M., Boomsma, Frans., Scholten, G., Wiegant,
1212 V.M., Nicholls, D.G., 1991. Differential release of amino acids, neuropeptides, and

1213 catecholamines from isolated nerve terminals. Neuron 6, 517–524.
1214 https://doi.org/10.1016/0896-6273(91)90054-4
1215 Wang, T., Liu, Y., Xu, X.-H., Deng, C.-Y., Wu, K.-Y., Zhu, J., Fu, X.-Q., He, M., Luo, Z.-G., 2011.
1216 Lgl1 Activation of Rab10 Promotes Axonal Membrane Trafficking Underlying
1217 Neuronal Polarization. Dev. Cell 21, 431–444.
1218 https://doi.org/10.1016/j.devcel.2011.07.007
1219 Wu, Y., Whiteus, C., Xu, C.S., Hayworth, K.J., Weinberg, R.J., Hess, H.F., Camilli, P.D., 2017.
1220 Contacts between the endoplasmic reticulum and other membranes in neurons.
1221 Proc. Natl. Acad. Sci. 114, E4859–E4867. https://doi.org/10.1073/pnas.1701078114
1222 Xu, H., Van Remmen, H., 2021. The SarcoEndoplasmic Reticulum Calcium ATPase (SERCA)
1223 pump: a potential target for intervention in aging and skeletal muscle pathologies.
1224 Skelet. Muscle 11, 25. https://doi.org/10.1186/s13395-021-00280-7
1225 Xu, X.-H., Deng, C.-Y., Liu, Y., He, M., Peng, J., Wang, T., Yuan, L., Zheng, Z.-S., Blackshear,
1226 P.J., Luo, Z.-G., 2014. MARCKS regulates membrane targeting of Rab10 vesicles to
1227 promote axon development. Cell Res. 24, 576–594.
1228 https://doi.org/10.1038/cr.2014.33